communications physics

Article

https://doi.org/10.1038/s42005-024-01926-w

$\mathbb{Z}/2$ topological invariants and the half quantized Hall effect

Check for updates

Bo Fu [1] ✉ & Shun-Qing Shen [2] ✉

The half-quantized Hall phase represents a unique metallic or semi-metallic state of matter characterized by a fractional quantum Hall conductance, precisely half of an integer v multiple of e^2/h. Here we demonstrate the existence of a $\mathbb{Z}/2$ topological invariant that sets the half-quantized Hall phase apart from two-dimensional ordinary metallic ferromagnets. The $\mathbb{Z}/2$ classification is determined by the line integral of the intrinsic anomalous Hall conductance, which is safeguarded by two distinct categories of local unitary and anti-unitary symmetries in proximity to the Fermi surface of electron states. We further validate the $\mathbb{Z}/2$ topological order in the context of the quantized Hall phase by examining semi-magnetic topological insulator Bi_2Te_3 and Bi_2Se_3 film for $v = 1$ and topological crystalline insulator SnTe films for $v = 2$ or 4. Our findings pave the way for future exploration and understanding of topological metals and their unique properties.

The classification of the electronic states according to topological invariants has revolutionized the understanding of quantum matter and the underlying quantum behaviors[1–9]. The $\mathbb{Z}$ and $\mathbb{Z}_2$ classifications have provided a robust framework to distinguish the topological insulating phases and superconducting phases from the many-body phases with a bulk energy gap[10–12]. The bulk-boundary correspondence, which lies at the heart of the topological insulating phases, asserts that the topological invariants of a material's bulk dictate the characteristics of its boundary states, leading to the discovery of a series of quantum phenomena and quantum materials in condensed matter.

The integer quantum Hall effect, characterized by a $\mathbb{Z}$ topological invariant in two dimensions, was first identified by Thouless, Kohmoto, Nightingale, and den Nijs (TKNN)[13,14]. They identified the integer v in quantum Hall conductivity $\sigma_H = ve^2/h$ as a topological invariant, derived from integrating the Bloch wave function over the Brillouin Zone (BZ). Due to its periodic boundary conditions, the first Brillouin zone of the electronic band is equivalent to the surface of a torus, where the integer v corresponds to the first Chern number of the surface curvature of the torus[15]. This Chern number sets an integer quantum Hall phase and quantum anomalous Hall phase from a simple band insulator. It is closely associated with the number of the gapless edge states on the system boundary, leading to the bulk-edge correspondence for the topological insulating phases[16]. Theoretical predictions and experimental observations of quantum anomalous Hall effect were one of the successful examples to explore the quantum state of matter in condensed matter[17–21]. A $\mathbb{Z}_2$ topological invariant was introduced by Kane and Mele[22] to characterize quantum spin Hall effect in systems with time-reversal symmetry. The $\mathbb{Z}_2$ index indicates the presence of a pair of helical edge states within the band gap around the system boundary, which are robust against time-reversal symmetry-preserving perturbations, such as non-magnetic disorder[23]. Thus, the $\mathbb{Z}$ and $\mathbb{Z}_2$ topological invariants distinguish topological phases from ordinary insulator. In early work[24], the topological classification of systems with time-reversal symmetry and space group symmetries was developed by examining the symmetry indicators at all high-symmetry points. Recent theoretical studies have advanced the field by providing a comprehensive topological classification of insulators protected by crystalline symmetries, based on K-theory[25,26] and symmetry indicators[27–30].

Unlike insulators, the anomalous Hall effect in ferromagnetic metals typically results in a non-quantized Hall conductivity. Haldane demonstrated that the anomalous Hall conductivity σ_{xy} in metallic ferromagnets can be described by the Berry connection $\mathbf{A}(\mathbf{k})$ over the Fermi surface loop C_μ: $\sigma_{xy} = \frac{e^2}{2\pi\hbar}\oint_{C_\mu} d\mathbf{l}\cdot\mathbf{A}(\mathbf{k})$[31]. However, the absence of a band gap in metallic ferromagnets raises questions about the feasibility of quantizing the anomalous Hall conductivity, in contrast to what is observed in the insulating state. Fu et al.[32] proposed the concept of a quantum anomalous semimetal, characterized by gapless Wilson fermions and a half-quantized Hall conductivity, indicative of a one-half topological invariant. Mogi et al. [33] observed this half-quantum Hall conductivity in a semi-magnetic topological insulator film, highlighting it as a signature of the parity anomaly in massive Dirac fermions. Zou et al. [34,35] analyzed the band structure of a magnetic topological insulator, identifying the presence of gapless Dirac fermions, which they linked to the quantization of the Hall conductivity. Since these discoveries, extensive research efforts have been directed towards understanding these effects[36–42]. Recently, the one-half topological number has also been proposed in the context of entangled quantum physics[43,44] and interacting systems[45,46].

[1]School of Sciences, Great Bay University, Dongguan, 523000 Guangdong Province, China. [2]Department of Physics, The University of Hong Kong, Pokfulam Road, Hong Kong, China. ✉e-mail: fubo@gbu.edu.cn; sshen@hku.hk

Table 1 | Symmetry constraint on Berry connection and Berry curvature

	Antiunitary ($\mathcal{A}$)				unitary ($\mathcal{U}$)			
χ	$+1$		-1		$+1$		-1	
Det[J]	$+1$	-1	$+1$	-1	$+1$	-1	$+1$	-1
$\oint_{C_\mu} d\mathbf{l}\cdot\mathbf{A}$ $\int_{\varepsilon<\mu} d^2\mathbf{k}\Omega_{xy}$	✓	×	×	$\begin{cases}\checkmark & N_{\text{tot}}=2N_\mu\\ \times & \text{otherwise}\end{cases}$	×	✓	$\begin{cases}\checkmark & N_{\text{tot}}=2N_\mu\\ \times & \text{otherwise}\end{cases}$	×
examples	T		$\mathcal{C}$				$\mathcal{S}$	

All symmetries are classified according to whether the symmetry is unitary ($\mathcal{U}$) or antiunitary ($\mathcal{A}$), the value of χ, and the determinant of the Jacobian matrix of the transformation Det[J] with $J_{\alpha\alpha'}=\frac{\partial(D\mathbf{k})_{\alpha'}}{\partial\mathbf{k}_\alpha}$. A ✓ indicates that the symmetry imposes a constraint such that the line integral of Berry connection is quantized and the Berry curvature integral over occupied states vanishes, while a × indicates there is no such constraint. We have exemplified time-reversal symmetry T, particle-hole symmetry $\mathcal{C}$, and chiral symmetry $\mathcal{S}$ in the last row.

Although the half-quantized Hall effect has been discussed in several specific systems, a comprehensive study that encompasses symmetry analysis, topological classification, and bulk-edge correspondence of this phenomenon is still lacking. In this article, we show that in metallic systems, if the electron states near the Fermi surface are invariant under a specific symmetry, the intrinsic Hall conductance must be quantized as a half-integer $\nu/2$ multiple of e^2/h. This leads to the $\mathbb{Z}/2$ topological invariant to distinguish the half quantized Hall phase from an ordinary metallic ferromagnet. We identified all possible symmetries that lead to this classification as listed in Tables 1 and 2. To obtain a nontrivial topological number, the global symmetry of the entire system must be broken. We thus introduce the concept of 'local symmetry', where a symmetry operation is applied only to a subspace of the entire Brillouin zone. The $\mathbb{Z}/2$ classification is based solely on the local symmetry of states at the Fermi surfaces, distinguishing from the $\mathbb{Z}$ and $\mathbb{Z}_2$ classifications for insulators and superconductors which depend on global band topology or symmetries. We provide a comprehensive classification of topological surface states, emphasizing how local symmetries influence the electronic properties of gapless Dirac cones. Additionally, we find that the derivative of the equilibrium circulating current with respect to the chemical potential corresponds to the number of conducting edge paths, thereby serving as a generalized form of bulk-edge correspondence for the system. Our findings are validated through tight-binding model calculations in the semi-magnetic heterostructures of topological insulators Bi_2Te_3 and Bi_2Se_3, as well as topological crystalline insulator SnTe films, which also suggest experimental pathways. Furthermore, we explore how extrinsic mechanisms are minimized by the presence of local symmetries, thereby stabilizing the Hall effect in $\mathbb{Z}/2$ topological metals.

Results

The main results of this study are summarized as follows: Consider a partially-filled band of a two-dimensional electronic lattice system. If the system Hamiltonian near the Fermi surface is invariant under one of the following symmetries—two unitary symmetries (C_{2x} and σ_v) and five antiunitary symmetries (T, IT, $C_{nz}T$, σ_hT, and $S_{nz}T$), as shown in Table 2—then the Hall conductivity is quantized to be a half-integer (including 0) multiple of e^2/h :

$$\sigma_H=\frac{\nu}{2}\frac{e^2}{h}. \tag{1}$$

Here, σ_v represents vertical mirror symmetry, C_{ni} denotes n-fold rotational symmetry about the i-axis, σ_h represents horizontal mirror symmetry, I denotes inversion symmetry, S_{nz} signifies n-fold improper rotational symmetry and T is the time-reversal symmetry.

Several remarks about Eq. (1) are made:

1. Zero Hall Conductivity ($\nu=0$): This occurs when the Hamiltonian of the entire system maintains one of these seven symmetries.
2. Non-zero Hall Conductivity ($\nu\neq 0$): For a non-zero ν, the symmetry is preserved locally near the Fermi surface but must be broken across the entire Brillouin zone.
3. Topological Invariant: These symmetries give rise to a $\mathbb{Z}/2$ topological invariant that characterizes the topological metallic or semi-metallic state, distinguishing the half-quantized Hall phase from conventional two-dimensional metals or semimetals.
4. Realization of Topological Semimetals: Due to the localized nature of surface states in topological insulator films, introducing symmetry-breaking perturbations in the bulk or on the opposing surface offers a natural platform to realize $\mathbb{Z}/2$ topological semimetal.
5. Bulk-Edge Correspondence: The half-quantization of the quantity $(e\partial J_{\text{edge}}/\partial\mu=\frac{\nu}{2}\frac{e^2}{h})$ for the circulating current corresponds to the number of conducting edge paths and can be interpreted as the bulk-edge correspondence for $\mathbb{Z}/2$ topological semimetal.

These findings provide a deeper understanding of the quantization of Hall conductivity in two-dimensional electronic systems and the associated topological properties.

Fermi-loop formula for Hall conductivity

We begin our discussion with the Kubo-Streda formula[47,48]. After disorder averaging[49,50], it encompasses both intrinsic and extrinsic contributions. Initially, we focus on the intrinsic part. For a two-dimensional electronic system, the Hall conductivity can be represented as[51]

$$\sigma_{xy}=\frac{e^2}{\hbar}\sum_n\int_{\text{BZ}}\frac{d^2\mathbf{k}}{(2\pi)^2}f_n(\mathbf{k})\Omega^n_{xy}(\mathbf{k}), \tag{2}$$

where the integral is carried out over the two-dimensional Brillouin zone (BZ). The function $f_n(\mathbf{k})$ denotes the occupation function. $\Omega^n_{xy}(\mathbf{k})$ is the Berry-curvature of band n, defined as $\Omega^n_{xy}=-2\text{Im}\langle\frac{\partial u_{n\mathbf{k}}}{\partial k_x}|\frac{\partial u_{n\mathbf{k}}}{\partial k_y}\rangle$ with $|u_{n\mathbf{k}}\rangle$ as the Bloch state. This result connects the Fermi sea transport contributions to the Berry curvature of the Bloch states which has been widely used to characterize the intrinsic Hall effect of bulk materials.

Applying the Stokes' theorem, the areal integral of the Berry curvature for the nth band over a specific region S_n in the Brillouin zone can be converted into a loop integral of the Berry connection $\mathbf{A}^n(\mathbf{k})$ along the oriented curve C_n that encloses S_n: $\int_{S_n}d^2\mathbf{k}\Omega^n_{xy}(\mathbf{k})=\int_{C_n}d\mathbf{l}\cdot\mathbf{A}^n(\mathbf{k})$. For a fully filled band, if the Berry connection $\mathbf{A}^n(\mathbf{k})$ is smoothly defined throughout the entire Brillouin zone, then S_n can encompass the whole Brillouin zone. In two dimensions, the Brillouin zone is topologically equivalent to a torus, which lacks a boundary. Consequently, the Chern number for nth band $\nu^n=\int_{\text{BZ}}d^2\mathbf{k}\Omega^n_{xy}(\mathbf{k})$ must be zero. Therefore, the presence of a non-zero Chern number presents a "topological obstruction" of a globally smooth gauge[52,53]. If $\mathbf{A}^n(\mathbf{k})$ exhibits a singularity, the Brillouin zone can be divided into two subregions, S^1_n and S^2_n, such that $\int_{\text{BZ}}=\int_{S^1_n}+\int_{S^2_n}$. Within each subregion, a smooth and continuous gauge is feasible. Across the boundary of these subregions, the Berry connection differs only by a gauge transformation, $\mathbf{A}^n_1(\mathbf{k})=\mathbf{A}^n_2(\mathbf{k})-\partial_{\mathbf{k}}\phi_n(\mathbf{k})$. The oriented loop C_n forming the boundary traverses S^1_n in the forward direction and S^2_n in the reverse direction. By utilizing Stokes' theorem to each subregion and adding the results, we find $\nu^n=\int_{\text{BZ}}d^2\mathbf{k}\Omega^n_{xy}(\mathbf{k})=\int_{C_n}d\mathbf{l}\cdot\partial_{\mathbf{k}}\phi_n(\mathbf{k})$. Because $\phi_n(\mathbf{k})$ is a unique function

Table 2 | List of symmetry constraint on the intrinsic Hall conductivity by the generators of magnetic point groups

	Unitary $\mathcal{U}$						Anti-unitary $\mathcal{A}$						
	I	C_{2x}	C_{nz}	σ_v	σ_h	S_{nz}	T	IT	$C_{2x}T$	$C_{nz}T$	σ_vT	σ_hT	$S_{nz}T$
All **k**	Nil	0	Nil	0	Nil	Nil	0	0	Nil	0	Nil	0	0
k = $\mathbf{k}_\mu$	Nil	$\frac{1}{2}\mathbb{Z}$	Nil	$\frac{1}{2}\mathbb{Z}$	Nil	Nil	$\frac{1}{2}\mathbb{Z}$	$\frac{1}{2}\mathbb{Z}$	Nil	$\frac{1}{2}\mathbb{Z}$	Nil	$\frac{1}{2}\mathbb{Z}$	$\frac{1}{2}\mathbb{Z}$

"All **k**" means that the Hamiltonian for all **k** is invariant under the symmetry while "**k** = $\mathbf{k}_\mu$" means that the Hamiltonian along the Fermi surface is invariant under the symmetry. "Nil" means that there is no symmetry constraint. I represent the inversion symmetry, which inverts all spatial coordinates. The notation $C_{n\alpha}$ denotes the n-fold rotational symmetries about the α-axis. The symbol σ_v represents vertical mirror symmetry, characterized by a mirror plane that includes the z-axis. Conversely, σ_h denotes horizontal mirror symmetry, featuring a mirror plane that is perpendicular to the z-axis.The notation $S_{nz} = C_{nz}\sigma_h$ defines an n-fold improper rotational symmetry. This operation consists of first performing a C_{nz} rotation about the z-axis, followed by a reflection in a plane that is perpendicular to the same axis. Lastly, T represents time reversal symmetry, which involves reversing the direction of time as well as other relevant physical quantities, such as magnetic fields and momenta.

on C_n, the resulting ν^n must be an integer. For a completely filled band, where the Brillouin zone is regarded as a closed manifold without boundary, the Chern number ν^n must be an integer, reflecting the topological quantization inherent to the fully filled band structure[13]. This leads to the $\mathbb{Z}$ classification of the topological insulators in two dimensions.

For a partially filled band, the integral over the occupied states forms an open manifold within the Brillouin zone, bounded by the curve C_μ corresponding to the sum of all the loops of the Fermi surface loops. Invoking Stokes' theorem, the Hall conductivity for this band can be recast as a loop integral over the Fermi surfaces:

$$\sigma_{xy}^n = \frac{e^2}{2\pi h}\oint_{C_\mu} d\mathbf{l}\cdot\mathbf{A}^n(\mathbf{k}). \tag{3}$$

In this situation $\oint_{C_\mu} d\mathbf{l}\cdot\mathbf{A}^n(\mathbf{k}) = \phi_n^{\mathrm{B}}$, which has the interpretation of a Berry phase. This equation elucidates the connection between the global property of the band structure encapsulated by the Berry curvature and the local geometric phases described by the Berry connection. It is critical to note that while determining ϕ_n^{B} using only the knowledge of the eigenstates $|u_{n\mathbf{k}}\rangle$ on the curve C_μ, there will exist a 2π ambiguity in comparison to the surface integral of the Berry curvature. The equation only holds precisely when a gauge choice is made that is smooth and continuous throughout the region S_n, including its boundary C_n, and this gauge is employed to calculate the loop Berry phase. In Beenakker's tangent fermion model[54], a singularity at $k = \pi$ precludes the straightforward application of the Berry connection formula. This singularity introduces complications that require a more subtle approach to accurately describe the system's topological properties.

Symmetry constraint on Berry curvature and Berry connection

According to Wigner's theorem, all symmetry operators can be categorized into one of two types: unitary or anti-unitary symmetry[55]. A unitary symmetry involves a transformation represented by a unitary operator $\mathcal{U}$, which satisfies the condition $\mathcal{U}\mathcal{U}^\dagger = \mathbb{I}$ where $\mathcal{U}^\dagger$ is the Hermitian adjoint of $\mathcal{U}$, and $\mathbb{I}$ is the identity operator.This unitary transformation preserves the norm of states as well as the angles between different quantum states. Crystalline symmetries such as rotations and reflections exemplify unitary symmetries. An antiunitary operator $\mathcal{A}$ is a combination of a unitary operator $\mathcal{U}$ and the complex conjugation operator $\mathcal{K}$, expressed mathematically as $\mathcal{A} = \mathcal{U}\mathcal{K}$. While antiunitary operations also preserve the norms of states, they do not maintain the phase of quantum states due to the complex conjugation. Antiunitary symmetry is commonly associated with time-reversal symmetry. In the following, we prove the half quantization of the Hall conductivity under the protection of the unitary and anti-unitary symmetry, respectively.

The anti-unitary symmetry. Consider a Bloch Hamiltonian $h(\mathbf{k})$ which is invariant under an anti-unitary symmetry $\mathcal{A} = \mathcal{U}\mathcal{K}$, *i.e.*,$\mathcal{A}h(\mathbf{k})\mathcal{A}^{-1} = \chi h(D\mathbf{k})$, where $\chi = \pm 1$ and $D\mathbf{k}$ is the transformed wave vector $\mathbf{k}$ under $\mathcal{A}$. Notably, $\chi = 1$ and $D\mathbf{k} = -\mathbf{k}$ indicate time-reversal symmetry, whereas $\chi = -1$ and $D\mathbf{k} = -\mathbf{k}$ denote particle-hole symmetry ($\mathcal{C}$). Due to this symmetry, the eigenstates of $h(\mathbf{k})$ at $\mathbf{k}$ and $D\mathbf{k}$ must be related by a gauge transformation. Explicitly, for any eigenstate $|u_{n\mathbf{k}}\rangle$ of $h(\mathbf{k})$ with eigenvalue $\varepsilon_{n\mathbf{k}}$ we have $h(D\mathbf{k})\mathcal{A}|u_{n\mathbf{k}}\rangle = \chi\mathcal{A}h(\mathbf{k})|u_{n\mathbf{k}}\rangle = \chi\varepsilon_{n\mathbf{k}}\mathcal{A}|u_{n\mathbf{k}}\rangle$. Thus $\mathcal{A}|u_{n\mathbf{k}}\rangle$ is an eigenstate of $h(D\mathbf{k})$ with the energy $\chi\varepsilon_{n\mathbf{k}}$. For $\chi = +1$, the symmetry connects two states with the same energy, while for $\chi = -1$ the symmetry connects two states with energies of opposite signs. We can expand $\mathcal{A}|u_{n\mathbf{k}}\rangle = \sum_m B_{n,m}(\mathbf{k})|u_{mD\mathbf{k}}\rangle$ where $B_{n,m}(\mathbf{k}) = \langle u_{mD\mathbf{k}}|\mathcal{A}|u_{n\mathbf{k}}\rangle$ is the sewing matrix. This matrix satisfies $BB^\dagger = \mathbb{I}$, and its elements are non-zero only when $\varepsilon_{n\mathbf{k}} = \chi\varepsilon_{m,D\mathbf{k}}$. Then the non-Abelian connections are related by a non-Abelian transformation

$$A_\alpha^{nn'}(\mathbf{k}) = -i\sum_m B_{n,m}(\mathbf{k})\partial_\alpha B_{m,n'}^\dagger(\mathbf{k}) - J_{\alpha\alpha'}\sum_{m,m'} B_{n,m}(\mathbf{k})\left[A_{\alpha'}^T\right]^{mm'}(D\mathbf{k})B_{m',n'}^\dagger(\mathbf{k}) \tag{4}$$

where $\alpha, \alpha' = x, y$ and $J_{\alpha\alpha'} = \frac{\partial(D\mathbf{k})_{\alpha'}}{\partial\mathbf{k}_\alpha}$ denotes element of the Jacobian matrix and T represents the transpose of a matrix. Then, the Berry curvature satisfies the condition

$$\Omega_{\alpha\beta}^{nn'}(\mathbf{k}) = -J_{\alpha\alpha'}J_{\beta\beta'}\sum_{m,m'} B(\mathbf{k})_{n,m}\left[\Omega_{\alpha'\beta'}^T\right]^{m,m'}(D\mathbf{k})B_{m',n'}^\dagger(\mathbf{k}). \tag{5}$$

For $\chi = +1$, all the labels m, m', n, n' denote occupied states. Conversely, for $\chi = -1$, the labels m, m' denote occupied states, and n, n' denote unoccupied states, or vice versa.

Now we consider the collection of Fermi surface loops C_μ which are invariant under the anti-unitary symmetry. These loops can be viewed as a subspace of the whole Brillouin zone. When performing the line integral of the Berry connection over these loops, it is necessary to sum over all states that share the same energy. For the two cases $\chi = \pm 1$, it can be expressed collectively as where $d\boldsymbol{l}$ are the differential vector element along the path C_μ

$$\oint_{C_\mu}\mathrm{Tr}_\mu[A_\alpha(\mathbf{k})]dl_\alpha = -i\oint_{C_\mu}\mathrm{Tr}_\mu[B(\mathbf{k})\partial_\alpha B^\dagger(\mathbf{k})]dl_\alpha - \oint_{DC_\mu}\mathrm{Tr}_{\chi\mu}[A_{\alpha'}(D\mathbf{k})]d(D\boldsymbol{l})_{\alpha'} \tag{6}$$

and we have used $J_{\alpha\alpha'}dl_\alpha = d(D\boldsymbol{l})_{\alpha'}$. The expressions $\mathrm{Tr}_{\chi\mu}[\ldots]$ denote the trace over the degenerate states at the energy $\chi\mu$.

We first discuss the case $\chi = +1$, where the right hand side of Eq. (6) involves the the occupides states. For an anti-unitary symmetry with $\mathrm{Det}[J] = +1$, the direction of integration along the path is preserved after the symmetry transformation (Fig. 1a). $\mathrm{Det}[J] = J_{xx}J_{yy} - J_{xy}J_{yx}$ is the determinant of the 2 × 2 Jacobian matrix. Consequently, we obtain: $\oint_{DC_\mu}\mathrm{Tr}_\mu[A_{\alpha'}(D\mathbf{k})]d(D\boldsymbol{l})_{\alpha'} = \oint_{C_\mu}\mathrm{Tr}_\mu[A_\alpha(\mathbf{k})]dl_\alpha$. Thus, the

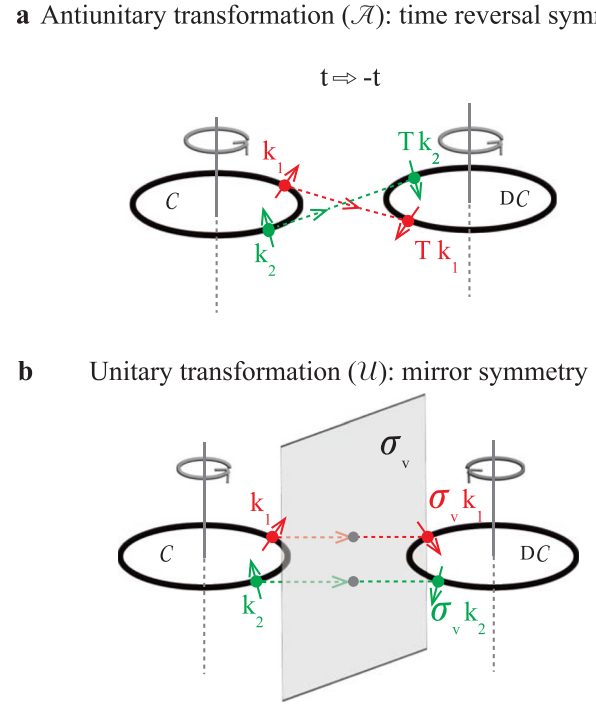

Fig. 1 | Schematic diagram of the effects of symmetry transformations. a Under time-reversal symmetry (T) transformation, the direction of the Fermi surface loop integral (black circle) is preserved, while the spin orientation of the states (arrows on the circle) is flipped. **b** Under mirror symmetry (σ_v) transformation, the direction of the loop integral is reversed, and the spin component parallel to the mirror plane is inverted, while the component perpendicular to the plane remains unchanged.

loop integral of the Berry connection is quantized to an half-integer multiple of 2π, i.e., $\oint_{C_\mu} \mathrm{Tr}_\mu[A_\alpha(\mathbf{k})]dl_\alpha = -i\frac{1}{2}\oint_{C_\mu} \mathrm{Tr}_\mu[B(\mathbf{k})\partial_\alpha B^\dagger(\mathbf{k})]dl_\alpha$. The sewing matrix $B(\mathbf{k})$ associated with the anti-unitary transformation $\mathcal{A}$ defines a continuous map from one dimensional circle(s) C_μ onto the unitary group $U(N_d)$, which is classified by the first homotopy group $\pi_1(U(N_d)) \cong \mathbb{Z}$. Here, N_d is the degree of the band degeneracy. Thus, the integral on the right hand side represents the winding number of the homotopic maps which leads to an integer ν multiple of 2π. Then, by combining with Eq. (3), we prove that when the states on the Fermi surface possess an anti-unitary symmetry with $\mathrm{Det}[J] = +1$, the Hall conductivity is equal to $\frac{\nu}{2}\frac{e^2}{h}$. It should be noted that the line integral of the Berry connection for the Hall conductivity is limited along the Fermi surface. Thus we do not require the whole system is invariant under the symmetry; the local symmetry on the Fermi surface is sufficient to constrain the Hall conductance. Alternatively, the Hall conductivity can be obtained by integrating the Berry curvature over Brillouin zone and tracing over all occupied states. If the whole system does possess such symmetry, from Eq.(5), we can derive: $\int d^2\mathbf{k}\epsilon_{\alpha\beta}\mathrm{tr}[\Omega_{\alpha\beta}(\mathbf{k})] = -\int d^2\mathbf{k}\mathrm{Det}[J]\epsilon_{\alpha'\beta'}\mathrm{tr}[\Omega_{\alpha'\beta'}(D\mathbf{k})]$ where we have utilized the relation $\epsilon_{\alpha\beta}J_{\alpha\alpha'}J_{\beta\beta'} = \epsilon_{\alpha'\beta'}\mathrm{Det}[J]$. The notation tr[…] indicates that the trace is taken over the occupied states. The transformation of the integration measure $\int d^2\mathbf{k}\mathrm{Det}[J] = \mathrm{sgn}(\mathrm{Det}[J])\int d^2(D\mathbf{k})$ results in $\{1 + \mathrm{sgn}(\mathrm{Det}[J])\}\int d^2\mathbf{k}\mathrm{tr}[\Omega_{xy}(\mathbf{k})] = 0$. Therefore, when $\mathrm{Det}[J] = +1$, the Hall conductivity vanishes, $\sigma_{xy} = 0$. Therefore, for $\chi = +1$, to have a nonzero ν in Eq. (1), there are two conditions: (i) there exist the local symmetry along the circle(s) of the Fermi surface; (ii) the symmetry of the whole system must be broken.

We then turn out attention to the case $\chi = -1$. Unlike the $\chi = +1$ scenario, the Berry connection integral on the right hand side of Eq. (6) includes states with a different energy $(-\mu)$. Consequently, we cannot determine the values of these terms by merely changing integral variables as in the $\chi = +1$ case. Therefore, in general, symmetries characterized by $\chi = -1$, such as particle-hole symmetry, do not impose constraints on the quantization of the Berry connection integral over the Fermi surface; additional conditions are necessary for definitive conclusions. Symmetries with $\chi = -1$ require an equal number of bands at positive and negative energies. The Hilbert space over all bands is topologically trivial; consequently, the trace of the Berry connection integral and the Berry curvature over all bands is necessarily trivial as well. When the total number of bands N_{tot} equals twice the number of bands intersected by the Fermi energy N_μ, i.e., $N_{tot} = 2N_\mu$, and considering the symmetry with $\mathrm{Det}[J] = -1$, the Berry connection integral, according to Eq. (6), becomes quantized as $\oint_{C_\mu} dl_\alpha \mathrm{Tr}_\mu[A_\alpha(\mathbf{k})] = 0$ or π mod 2π, analogous to $\mathbb{Z}_2$ classification in symmetry class D in one dimension. It leads to a $\mathbb{Z}/2$ classification of hall conducitivity. If all the occupied states satisfy this symmetry, it can be demonstrated that the integral of the Berry curvature must be zero. On the other hand, symmetries characterized by $\mathrm{Det}[J] = +1$ impose no constraints on these quantities. Regarding particle-hole symmetry, it is characterized by $\mathrm{Det}[J] = +1$ in a 2D system, not $\mathrm{Det}[J] = -1$ as in a purely 1D system, thus imposing no constraint.The Fermi surface loop which can be viewed as a one-dimensional manifold embedded within a two-dimensional Brillouin zone differs from a purely 1D system.

The unitary symmetry. For a unitary symmetry $\mathcal{U}$, the Bloch Hamiltonian has the relation $\mathcal{U}h(\mathbf{k})\mathcal{U}^{-1} = \chi h(D\mathbf{k})$. Crystalline symmetries, such as reflection and rotation, exemplify the case where $\chi = +1$. Conversely, when $\chi = -1$ and $D\mathbf{k} = \mathbf{k}$, the symmetry denotes the chiral symmetry. The sewing matrix can be expressed as $B_{n,m}(\mathbf{k}) = \langle u_{mD\mathbf{k}}|\mathcal{U}|u_{n\mathbf{k}}\rangle$.Then, the Berry connection has the following property:

$$A_\alpha^{nn'}(\mathbf{k}) = -i\sum_m B_{n,m}^*(\mathbf{k})\partial_\alpha B_{m,n'}^T(\mathbf{k}) + J_{\alpha\alpha'}\sum_{m,m'} B_{n,m}^*(\mathbf{k})A_{\alpha'}^{mm'}(D\mathbf{k})B_{m',n'}^T(\mathbf{k}) \tag{7}$$

and the non-Abelian Berry curvature satisfies

$$\Omega_{\alpha\beta}^{nn'}(\mathbf{k}) = J_{\alpha\alpha'}J_{\beta\beta'}\sum_{m,m'} B_{n,m}^*(\mathbf{k})\Omega_{\alpha'\beta'}^{mm'}(D\mathbf{k})B_{m',n'}^T(\mathbf{k}). \tag{8}$$

Compared with Eq. (4) and Eq. (6), an additional minus sign appears in the transformed results due to the absence of the complex conjugation operator. In the case of $\chi = +1$, if the Fermi surface loops exhibit symmetries with $\mathrm{Det}[J] = -1$, the Berry connection line integral over these loops is quantized as a half-integer multiplied by 2π, i.e., $\sigma_{xy} = \frac{\nu}{2}\frac{e^2}{h}$. The direction of integration along the path is reversed after the symmetry transformation, as shown in Fig. 1b. Moreover, if all occupied states exhibit this symmetry, the integral of the Berry curvature over these states vanishes, resulting in $\sigma_{xy} = 0$. In the case of $\chi = -1$, symmetries relate states with opposite energies therefore generally imposes no constraints on the quantization of these quantities. A special case arises when $N_{tot} = 2N_\mu$. In this scenario, when $\mathrm{Det}[J] = +1$, the Berry connection line integral will be quantized and Berry curvature integral vanishes. the Berry connection line integral will be quantized, and the Berry curvature integral vanishes. Chiral symmetry ($\mathcal{S}$) exemplifies this type of symmetry. Systems exhibiting chiral symmetry belong to symmetry class AIII in the Altland-Zirnbauer classification. In one dimension, the topological invariant is of type $\mathbb{Z}$ and is characterized by an integer-valued winding number w. The Berry connection integral is related to this number by the relation $\oint_{C_\mu} \mathrm{Tr}_\mu[A_\alpha(\mathbf{k})]dl_\alpha = \mathrm{mod}(w, 2)\pi$. When $\mathrm{Det}[J] = -1$, there is no such constraint.

Local symmetry via global symmetry breaking

Equations (3) and (21) indicate that the calculation of the anomalous Hall conductivity in metals can be reduced to an evaluation at the Fermi surface by means of Stokes's theorem. This formula prompts us to introduce the concept of local symmetry. Local symmetry is defined as a symmetry that applies solely to the states at and near the Fermi surface rather than to the entire state space. The proposed local-symmetry represents departure from traditional symmetries in physics that generally apply to the whole system

under consideration. Based on the symmetry analysis in the previous section, when the chemical potential varies within the region exhibiting the seven types of local symmetries in Table 2, the Hall conductivity will display a plateau. The presence of the local symmetry ensures that the half-quantized Hall conductivity is immune to weak disorder or interactions, thereby stabilizing the quantized Hall metallic phase, instead of it being a transient critical point between two insulating phases.

Local symmetry in accidental cases. We first present two examples to illustrate how the presence of local symmetry can lead to the half-quantization of the Hall conductivity in two two-band models. The first example is the Qi-Wu-Zhang(QWZ) model for a Chern insulator. The $k \cdot p$ Hamiltonian is expressed as $H_{\mathrm{BHZ}} = \hbar v \mathbf{k} \cdot \boldsymbol{\sigma} + (\Delta - b\hbar^2\mathbf{k}^2)\sigma_z$ with $\mathrm{sgn}(\Delta b) > 0$[12]. Its Hall conductivity as a function of the chemical potential is given by $\sigma_H = \frac{e^2}{2h}[\frac{\Delta - b\hbar^2 k_F^2}{\mu} + \mathrm{sgn}(b)]$ where k_F as the Fermi wave vector. As the mass term goes to zero, $\Delta - b\hbar^2 k_F^2 = 0$, the time-reversal symmetry or the parity symmetry along the Fermi surface loop is restored, and the Hall conductivity becomes a half-integer value of $\frac{e^2}{2h}\mathrm{sgn}(b)$. However, the total system still breaks the time-reversal symmetry. This example illustrates explicitly that the local symmetry can be realized while the whole system breaks the symmetry, and can be regarded as a typical example of local symmetry. Recent observed one-half anomalous Hall effect in twisted systems is possibly relevant to this mechanism[56,57].

The second example is the massless Wilson fermion by setting $\Delta = 0$. It breaks the time reversal symmetry in the presence of the $b\hbar^2\mathbf{k}^2$ term. In the low-energy limit, the system can be regarded approximately as by linear Dirac fermions as the the symmetry broken term almost vanishes. The parity symmetry is restored when the chemical potential approaches the Dirac point. Consequently, the Hall conductivity is reduced to $\frac{e^2}{2h}\mathrm{sgn}(b)$. This is also an example of local symmetry near the Dirac point[32].

This argument can be generalized to the cases where the local symmetry is approximately preserved. For instance, consider a two-dimensional free electron gas with the Rashba spin-orbit coupling subjected to a Zeeman effect: $H_{\mathrm{R}} = \frac{\hbar^2|\mathbf{k}|^2}{2m} + \lambda \mathbf{k} \cdot \boldsymbol{\sigma} + \frac{\mu_B g}{2} B_z \sigma_z$ where m is the effective mass, λ is the linear Rashba coupling, μ_B is the Bohr magneton, and g is the Landé g-factor[51,58,59]. When the chemical potential is located within the Zeeman-induced energy splitting, the Fermi surface is a single loop. The Hall conductivity is given by: $\frac{e^2}{2h}[\frac{\mu_B g B_z/2}{\mu - \hbar^2 k_F^2/2m} - \mathrm{sgn}(B_z)]$. In the case where $\mu_B g B_z \ll \frac{2m\lambda^2}{\hbar^2}$ the symmetry-breaking term is negligibly small, and the Hall conductivity approximately equals to $-\mathrm{sgn}(B_z)\frac{e^2}{2h}$.

Local symmetries in the surface states of three-dimensional topological insulators. In the scenarios described above, the condition to exhibit a half-integer Hall conductivity is typically regarded as an accident occurrence, often necessitating fine-tuning. We now turn to thin films of three-dimensional topological (crystalline) insulator systems. These films host gapless surface states at terminations due to the bulk's inherent topological characteristics[60–65]. Purely 2D systems typically suffer from a fermion-doubling problem[66] that a single Kramers degeneracy in momentum space must always have a counterpart elsewhere in the Brillouin zone. Unlike the purely 2D systems, films of three-dimensional topological (crystalline) insulators allow Kramers pairs to exist isolated on a single two-dimensional (2D) surface[60,61]. The surface states of topological insulator are localized near the two surfaces and these pairs are connected across the 3D bulk, with their counterparts on the opposite surface, respectively.

Understanding crystal symmetry and its manifestation in the projected surface Brillouin zone is crucial in studying surface phenomena in three-dimensional topological systems[67,68]. With the surface termination, the three-dimensional symmetry of the bulk crystal is reduced, affecting the surface states and its electronic structure. All 2D nonmagnetic surfaces adhere to one of the 17 wallpaper groups. The spatial wallpaper group symmetries are limited to those 3D space group symmetries that preserve the surface normal vector, including rotations around that vector, in-plane lattice translations, mirror reflections, and glide reflections.The surface Brillouin zone is derived by projecting the three-dimensional Brillouin zone onto a plane aligned with the surface orientation. This projection typically results in a two-dimensional representation of the 3D Brillouin zone with some inherited symmetries, though generally with reduced symmetry due to the surface's lower symmetry relative to the bulk. The center of the surface Brillouin zone ($\bar{\Gamma}$ point) typically maintains the full symmetry of the wallpaper group. The other high-symmetry points in the surface Brillouin zone (like the $\bar{X}$,$\bar{M}$ points) do not exhibit the full symmetry of the wallpaper group but have a subgroup of the full group's symmetry.

Local symmetry by magnetic doping. In three-dimensional topological (crystalline) insulator films, the seven symmetries in Table 2 can be categorized into two types: (i) σ_v, T, and $C_{nz}T$ which map one surface onto itself; and (ii) C_{2x}, IT, $S_{nz}T$, and $\sigma_h T$, which map one surface to the opposite surface. Due to the localized nature of the surface states, symmetry-breaking perturbations in the bulk–such as magnetic doping in the middle layers–affect primarily the high-energy states and have minimal impact on the gapless surface states, thus preserving the local symmetry of the surface states. Similarly, perturbations affecting one surface have minimal impact on the states at the opposing surface. By selectively broken symmetries to open an energy gap in the surface state on one side[33,69,70], while ensuring that the Fermi energy intersects the gapless surface state on the opposing side, the local symmetry can survive. Thus, this provides a possible and feasible platform for realizing quantized Hall metal states protected by local symmetry.

Firstly, we consider the introduction of magnetic doping in the middle of the film, ensuring that both surface states remain gapless, as diagrammatically depicted in Fig. 2a. In this scenario, the surface states retain all the symmetries of the undoped 3D bulk. Therefore, if the undoped 3D bulk exhibits any one of the seven symmetries, the surface states in the doped film also preserve this local symmetry. As demonstrated in ref. 71, when the magnetic doping in the middle layers exceeds a critical strength, the system can exhibit nonzero Hall conductivity with a half-quantized plateau characterized by $|\nu| = 2$. Next, we consider the application of magnetic doping on one surface to induce an energy gap in the surface states, as illustrated diagrammatically in Fig. 2b. In this case, the type (ii) local symmetries for surface states are disrupted, leaving only type (i) local symmetries intact. As demonstrated in refs. 34,35, in semimagnetic topological insulator films, the Hall conductivity becomes half-quantized at $|\nu| = 1$ when the chemical potential intersects only the gapless surface state, a condition preserved by the presence of local T symmetry[34,35]. Finally, we consider an axion state where an out-of-plane Zeeman term with opposite directions is applied to both surfaces[72–76], as shown in Fig. 2c. In this arrangement, the Zeeman field applied in the z-direction breaks all type (i) local symmetries but preserves type (ii) symmetries if the amplitudes of these Zeeman terms are identical. Therefore, in this situation, when the chemical potential sweeps over the gapped surface states, the Hall conductivity remains half-quantized.

Classification of the single gapless Dirac cone with symmetry C_n and T

In this section, we explore the constraints imposed on the form of surface states at high-symmetry points within the surface Brillouin zone, arising from the presence of T and C_n. We then explore how the generalized no-go theorem, which typically prevents the existence of a single gapless Dirac cone with a nonzero topological number throughout the entire Brillouin zone in lattice systems, can be circumvented by introducing symmetry-breaking elements.

Characteristics of surface states under both C_{nz} and T symmetries. The surface states Hamiltonian in general has the following 2×2 form

$$H(\mathbf{k}) = f(\mathbf{k})\sigma_+ + f^*(\mathbf{k})\sigma_- + g(\mathbf{k})\sigma_z \tag{9}$$

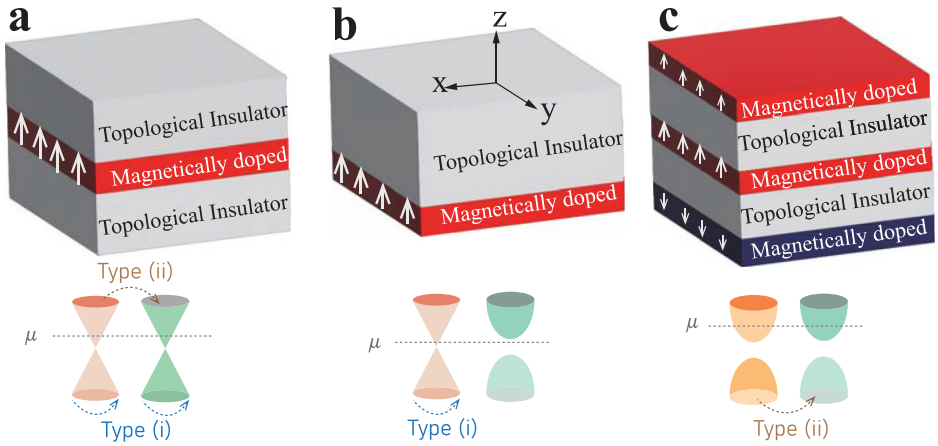

Fig. 2 | Local symmetries in the surface states of three-dimensional topological insulator films. Topological insulator film with different magnetic doping scenarios to illustrate the local symmetries at the Fermi surface μ. The red and blue regions illustrate the areas of magnetic doping in the samples. The white arrows indicate the magnetization direction. Orange cones denote the top surface states while green cones represent the bottom surface states. The black dashed lines indicate the position of the Fermi surface. **a** Magnetic doping in the middle layers. Both type (i) local symmetries, which map one surface onto itself, and type (ii) local symmetries, which map one surface to the opposite surface, are preserved. **b** Semimagnetic film with magnetic doping on bottom surface. Only type (i) symmetries are preserved. **c** Axion state with magnetic doping applied to both surfaces, where the exchange fields point in opposite directions. This configuration preserves only type (ii) symmetries when the amplitudes of the Zeeman fields are equal.

where $\sigma_\pm = (\sigma_x \pm i\sigma_y)/2$ and f and g are complex and real functions of $\mathbf{k}$, respectively. Depending on whether the surface states are spin 1/2 or spinless particles, symmetry constraints dictate different forms for f and g. Table 3 offers an overview of the symmetry-permitted forms of $f(\mathbf{k})$ and $g(\mathbf{k})$ for small $\mathbf{k}$. A detailed analysis is available in the Methods section.

For spin 1/2 case, g vanishes if the system possesses a 2-fold rotational symmetry axis. In systems exhibiting C_{3z}, such as Bi_2Se_3, Bi_2Te_3, a hexagonal warping term $(v'k_+^3 + v'^*k_-^3)\sigma_z$ is allowed by symmetry[77,78]. This leads to an energy dispersion that deviates from a circular shape, often producing a snowflake-like pattern. However, the presence of time reversal symmetry ensures that the line integral of Berry connection along the loop of a constant energy for such a system remains quantized to π, thereby upholding the half quantization of Hall conductivity in a semi-magnetic Bi_2Se_3 film. For Qi-Wu-Zhang model with C_{4z} symmetry, such a warping term is excluded by symmetry[79,80].

For spinless case, when $m_e = 0$, the leading term of $f(\mathbf{k})$ is a constant. To properly reflect the momentum dependence, $f(\mathbf{k})$ should be expanded to include higher order terms of $\mathbf{k}$. In this case, the surface states at the high-symmetry point $\mathbf{k}$ is split into n Dirac cones with linear dispersion at generic momenta $\mathbf{k}_0, C_{nz}\mathbf{k}_0, \ldots, C_{nz}^{n-1}\mathbf{k}_0$ with $f(\mathbf{k}_0) = 0$. For instance, when examining the case where $n = 2$, we limit our consideration to the second lowest order of $\mathbf{k}$: $f(\mathbf{k}) = v + v_+k_+^2 + v_-k_-^2$ [81]. Given that $f(\mathbf{k}_0) = 0$, the presence of 2-fold rotational symmetry necessitates that $f(-\mathbf{k}_0) = 0$ as well. We can then expand $f(\mathbf{k})$ in the vicinity of $\pm\mathbf{k}_0$, with $\mathbf{k} = \pm\mathbf{k}_0 + \delta\mathbf{k}$, such that $f_\pm(\mathbf{k}) \simeq \pm 2(v_+k_{0+}\delta k_+ + v_-k_{0-}\delta k_-)$. Therefore, the winding number w around the two Dirac points is of the same sign, which leads to a total winding number expressed as $2\mathrm{sgn}(|v_-| - |v_+|)$. When $m_e \neq 0$, the leading term of $f(\mathbf{k})$ is proportional to $|\mathbf{k}|^2$, resulting in quadratic dispersion. An examples of this is the Fu model[63], where the quadratic band touching is linked with a two-fold degeneracy enforced by 2D representations for $n = 4$.

The generalized no-go theorem. When the gapless cone, as shown in Table 3, is implemented on a lattice while preserving time-reversal symmetry, it encounters the fermion doubling problem. For systems with 2-fold rotational symmetry (e.g., including 2, 4, 6-fold symmetries), an additional chiral symmetry for the surface states allows us to define a winding number for a 1D integral path over the Fermi loop, which is a $\mathbb{Z}$-type invariant[8]. However, in systems exhibiting three-fold rotational symmetry, where chiral symmetry is absent, the Berry phase along any closed loop with local time-reversal symmetry preserved is quantized. This Berry phase represents a $\mathbb{Z}_2$-type invariant, as it is defined only up to multiples of 2π[82]. A stable topological point at $\mathbf{k}$ is characterized by a non-zero topological invariant, which can be either $\mathbb{Z}$ or $\mathbb{Z}_2$. A non-zero topological invariant for a 1D integral path corresponds to a topological charge enclosed by the loop. The generalized no-go theorem is that the sum of the topological charges carried by the topological points across the entire Brillouin Zone must cancel out, achieving charge neutralization[83,84]. For system with C_3 symmetry, when the Berry phase is π corresponding $\mathbb{Z}_2 = 1$, an additional Dirac cone is required to offset this charge neutralization discrepancy. For system with 2-fold rotational symmetry, any topological point with a nonzero winding number must be paired with another topological point that has an opposite winding number[66,85].

In order to maintain a single gapless structure in Eq. (9) at low energy scales and to avoid the fermion doubling problem, time-reversal symmetry must be explicitly broken in the high energy regime. We consider a Hamiltonian of the form $H(\mathbf{k}) = f(\mathbf{k})\sigma_+ + f^*(\mathbf{k})\sigma_- + m(\mathbf{k})\sigma_z$ with $m(\mathbf{k}) = g(\mathbf{k})$ in the low energy regime and $m(\mathbf{k}) = V_z$ in the high energy regime which breaks time-reversal symmetry explicitly[34,35]. The wave function for the valence band is given by $|u_\mathbf{k}^-\rangle = \left(-\sin(\varphi/2)e^{i\mathrm{Arg}[f]}, \quad \cos(\varphi/2)\right)^T$ for $V_z > 0$ and $|u_\mathbf{k}^-\rangle = \left(-\sin(\varphi/2), \quad \cos(\varphi/2)e^{-i\mathrm{Arg}[f]}\right)^T$ for $V_z < 0$ to ensure that the wave function is singularity-free throughout the Brillouin zone. Here, $\cos\varphi = m/\epsilon$ with $\epsilon = \sqrt{|f|^2 + m^2}$. Subsequently, the Hall conductivity can be calculated as,

$$\sigma_{xy} = \frac{e^2}{2h}\int_{C_\mu} d\mathbf{l}\cdot\{\mathrm{sgn}(V_z)\partial_\mathbf{k}\mathrm{Arg}[f] - \frac{g}{\epsilon}\partial_\mathbf{k}\mathrm{Arg}[f]\} \tag{10}$$

where the first term simplifies to $\frac{e^2}{2h}\mathrm{sgn}(V_z)w$ and the second term vanishes due to the property that $g(\mathbf{k}_\mu) = -g(-\mathbf{k}_\mu)$ under time reversal symmetry. This result indicates the Hall conductivity for each type of Dirac fermion listed in Table 3, resulting from the introduction of the time-reversal symmetry-breaking term.

Bulk-edge correspondence

Bulk-edge correspondence is a fundamental concept in topological phases of matter that links boundary phenomena to the bulk's topological properties. In the integer (anomalous) quantum Hall effect, the quantization of Hall conductance is determined by an integer topological invariant known as the Chern number, which specifies the number of chiral edge states. In $\mathbb{Z}/2$ topological semimetal, where there is no well-defined band gap, the nature of the bulk-edge correspondence becomes a critical question. Here, we determine that the quantity $e\partial J_{\mathrm{edge}}/\partial\mu$ for the equilibrium circulating current J_{edge} corresponds to the number of conducting edge paths, thereby serving as a generalized form of bulk-

Table 3 | Summary of the classification of the gapless surface states under C_{nz} and T

spin $\frac{1}{2}$					spinless				
n	m_o	$f(\mathbf{k})$	$g(\mathbf{k})$	examples	$\sigma_{xy}[\frac{e^2}{2h}\mathrm{sgn}(V_z)]$	m_e	$f(\mathbf{k})$	$g(\mathbf{k})$	examples	$\sigma_{xy}[\frac{e^2}{2h}\mathrm{sgn}(V_z)]$
2	1	$v_+k_+ + v_-k_-$	0		$\mathrm{sgn}(\lvert v_-\rvert - \lvert v_+\rvert)$	0	$v + v_+k_+^2 + v_-k_-^2$	0	SnTe[84]	$2\mathrm{sgn}(\lvert v_-\rvert - \lvert v_+\rvert)$
3	0	$v_+k_+^3 + v_-k_-^3$	$\mathrm{Re}(v'k_+^3)$		$3\mathrm{sgn}(\lvert v_-\rvert - \lvert v_+\rvert)$	0	$v + v_+k_+^6 + v_-k_-^6$	$\mathrm{Re}(v'k_+^3)$		$6\mathrm{sgn}(\lvert v_-\rvert - \lvert v_+\rvert)$
3	1	vk_-	$\mathrm{Re}(v'k_+^3)$	$Bi_2Se(Te)_3$[87]	$+1$	1	vk_+^2	$\mathrm{Re}(v'k_+^3)$		-2
3	2	vk_+	$\mathrm{Re}(v'k_+^3)$		-1	2	vk_-^2	$\mathrm{Re}(v'k_+^3)$		$+2$
4	1	vk_-	0	QWZ model[11]	$+1$	0	$v + v_+k_+^4 + v_-k_-^4$	0		$4\mathrm{sgn}(\lvert v_-\rvert - \lvert v_+\rvert)$
4	3	vk_+	0		-1	2	$v_+k_+^2 + v_-k_-^2$	0	Fu model[63]	$2\mathrm{sgn}(\lvert v_-\rvert - \lvert v_+\rvert)$
6	1	vk_+	0		-1	0	$v + v_+k_+^6 + v_-k_-^6$	0		$6\mathrm{sgn}(\lvert v_-\rvert - \lvert v_+\rvert)$
6	3	$v_+k_+^3 + v_-k_-^3$	0		$3\mathrm{sgn}(\lvert v_-\rvert - \lvert v_+\rvert)$	2	vk_+^2	0		-2
6	5	vk_-	0		-1	4	vk_-^2	0		$+2$

The first column specifies the order of rotation, denoted by n. The second column represent $m_o = \mathrm{mod}(2l+1, n)$ with l as the orbital angular momentum for the first basis state. Columns three through five represent the symmetry allowed functions $f(\mathbf{k})$ and $g(\mathbf{k})$ at the lowest order of $\mathbf{k}$ (if the lowest order is $\mathbf{k}$-independent, we truncate to the second lowest order), and the examples for spin 1/2 system. Column six indicates half quantized Hall conductivity corresponding to each case in the presence of magnetization V_z. The subsequent five columns provide equivalent information for spinless system. The subsequent five columns provide equivalent information for spinless system with $m_e = \mathrm{mod}(2l, n)$. The coefficients $v, v_\pm$ within $f(\mathbf{k})$ are complex.

edge correspondence for the system. The circulating current can be evaluated by considering a ribbon geometry with an open boundary in the x direction and a periodic boundary condition in the y-direction. The circulating current J_{edge} in y-direction can be calculated by integrating the current density $j_y(x)$ from one boundary at x_{edge} to an interior position x_{bulk} within the bulk region, $J_{\mathrm{edge}} = \int_{x_{\mathrm{edge}}}^{x_{\mathrm{bulk}}} dx j_y(x)$. J_{edge} is expected to converge quickly as the distance $\Delta x = |x_{\mathrm{edge}} - x_{\mathrm{bulk}}|$ increases. For a $\mathbb{Z}/2$ topological semimetal with $\sigma_{xy} = (\nu/2)(e^2/h)$, we have $e\partial J_{\mathrm{edge}}/\partial\mu = (\nu/2)(e^2/h)$ which indicates that there are $\nu/2$ conducting edge paths with each contributing one quantum of condutance e^2/h. As demonstrated by previous work[34], we explore the bulk-edge correspondence of a $\mathbb{Z}/2$ topological semimetal with $\nu = 1$. In this scenario, the system features a single gapless Dirac cone; there are no well-defined edge states, and the edge current is collectively carried by all extended bulk states beneath the Fermi surface. Additionally, $e\partial J_{\mathrm{edge}}/\partial\mu = (1/2)(e^2/h)$ in the thermodynamic limit, where the "1/2" edge conducting path is contribued by all the bulk states. A recent study reveals that a 1/2 topological semimetal can also host localized states at the boundary under specific conditions[86]. These localized modes correspond to a single edge channel, contributing one quantum of conductance. Detailed numerical calculations verify that the bulk state provides another counterpropagating $-1/2$ edge path, resulting in a net 1/2 outcome.

For topological semimetals with a high topological number, $|\nu| \geq 2$, there are conventional cases where the system may be viewed as a simple combination of a topological Chern insulator by a conventional metal or topological metal with a lower topological number. Here we focus exclusively on the unconventional cases that cannot be decomposed. To illustrate this, we consider the case where $(n, m_e) = (4, 2)$ and $\nu = 2$ as an example. Up to a gauge transformation, the form of the $k \cdot p$ Hamiltonian is determined by symmetry considerations: $H = t_x(k_x^2 - k_y^2)\sigma_x + 2t_y k_x k_y \sigma_y$. We perform a tight-binding calculation to examine the boundary effects in this model. To implement the gapless Dirac fermion on a lattice and avoid fermion doubling, we introduce a T symmetry breaking term $t_z|\mathbf{k}|^4\sigma_z$. The simulation results are detailed in Supplementary Note 1. In the model we studied, there exists localized states at the boundaries (Supplementary Fig. 1b, c)that is responsible for the integer quantization of $\partial J_{\mathrm{edge}}/\partial\mu = \pm e/h$. The contribution from the bulk states can be neglected, as evidenced by comparing the blue and red lines, which correspond to the contributions from the localized states and the total result, respectively, in Supplementary Fig. 1d.

Overall, the half-quantization of the quantity $e\partial J_{\mathrm{edge}}/\partial\mu = (\nu/2)(e^2/h)$ for the circulating current corresponds to the number of conducting edge paths and can be viewed as the bulk-edge correspondence in $\mathbb{Z}/2$ topological metals with $\sigma_{xy} = (\nu/2)(e^2/h)$. This quantization can be attributed to bulk states, localized edge states, or both, depending on specific conditions. Each scenario should be analyzed on a case-by-case basis to understand the underlying mechanisms fully.

Two materials

In this section, we numerically validate the discussions presented above by examining semi-magnetic films of the strong topological insulators Bi_2Te_3 and Bi_2Se_3, as well as the topological crystalline insulator SnTe. We show that $\nu = 1$ for Bi_2Te_3 and Bi_2Se_3 and $\nu = 2$ or 4 for SnTe.

Strong topological insulators Bi_2Te_3 and Bi_2Se_3. The strong three-dimensional (3D) topological insulators (TIs), Bi_2Te_3 and Bi_2Se_3, exhibit a rhombohedral crystal structure that falls within the R3m space group (No. 166)[78,87]. To compute the electronic structure of a TI film, we employ a tight-binding model encompassing four states, specifically, $|P1_-^+, \pm\frac{1}{2}\rangle$ and $|P2_+^-, \pm\frac{1}{2}\rangle$, with parameters determined by fitting to electronic properties derived from first-principles calculations[88]. The Hamiltonian's form is significantly constrained by crystal symmetries and time-reversal symmetry, characterized by: i) threefold rotation symmetry C_{3z} along the z axis, ii) twofold rotation symmetry C_{2x} along the x axis, iii) inversion symmetry I, and iv) time-reversal symmetry T. Figure. 3a illustrates the

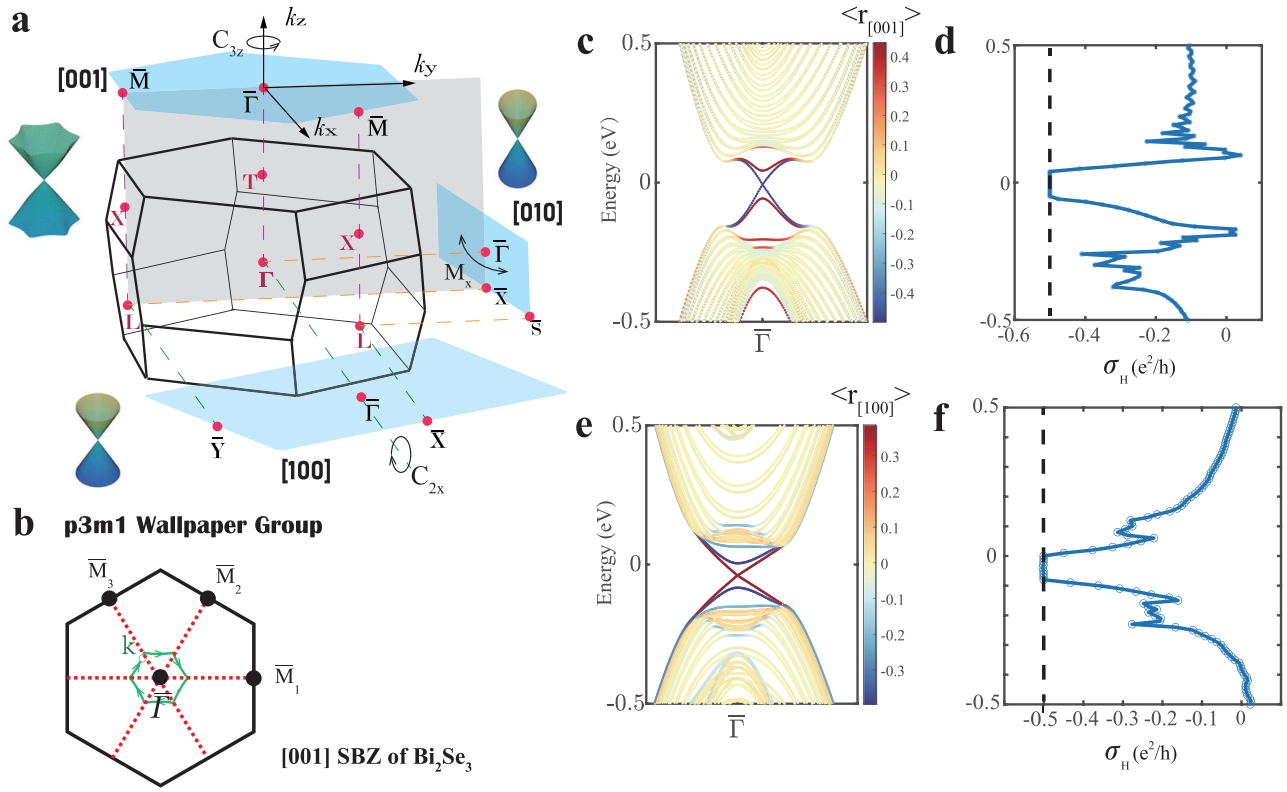

Fig. 3 | The half-quantized Hall phase in strong topological insulators. **a** Illustration of high-symmetry points within the 3D Brillouin zone, the projected surface Brillouin zones (denoted by the blue surfaces) for the [001], [100] and [010] surfaces of the rhombohedral structure, and the Dirac surface states at $\bar{\Gamma}$ points for various terminations. The black lines indicate the boundary of the Brillouin zone and the solid dots indicate time-reversal-invariant points. **b** The surface Brillouin zone (SBZ) for the [001] termination. The black lines mark the boundaries of the Brillouin zone, the solid dots represent time-reversal-invariant points, and the red dashed lines represent mirror lines. The green line indicates the Fermi surface loop. Panels **c** and **d** depict the slab band structure and Hall conductivity σ_H as a function of chemical potential μ for the [001] termination with a time-reversal symmetry breaking term added on one surface ($\langle r_{[001]}\rangle \sim 0.5$), respectively, while panels **e** and **f** are the corresponding results for the [100] termination with a time-reversal symmetry breaking term added on one surface ($\langle r_{[100]}\rangle \sim -0.5$). Parameters: $\frac{\mu_B}{2} g_{1z} B_z = 0.05$eV for panels **c** and **d**; $\frac{\mu_B}{2} g_{2x} B_x = 0.05$eV for panels **e** and **f**. The tight-binding model and its parameters are the same as those described in ref. 42.

3D Brillouin zone and the surface Brillouin zones for the [001], [100], and [010] surfaces of the rhombohedral structure, each featuring a single Dirac cone. However, their properties vary considerably due to different symmetries. The 2D surface for a [001] termination adheres to wallpaper group $p3m1$, and the surface Brillouin zone features a single Dirac cone at $\bar{\Gamma}$, leading to a single ring structure in the Fermi loop as illustrated in Fig. 3b. A hexagonal warping term allowed by C_{3z} symmetry results in a non-circular, snowflake-like energy dispersion. For the [100] surface, the warping term is precluded by C_{2x} symmetry. For the [010] surface, which possesses only mirror symmetry σ_v (depicted by the shaded plane in Fig. 3a), the lowest-order momentum term allowed in $g(\mathbf{k})$ is linear.

By introducing a time-reversal symmetry-breaking Zeeman term on one surface of the [001] and [100] terminations[89],

$$H' = \sum_{\mathbf{r}} \psi^{\dagger}_{\mathbf{r}} f(\mathbf{r}) \frac{\mu_B}{2} \sum_{i=x,y,z} [g_{1i} B_i \tau_0 \sigma_i + g_{2i} B_i \tau_z \sigma_i] \psi_{\mathbf{r}} \qquad (11)$$

where the creation field operator $\psi^{\dagger}_{\mathbf{r}} = (c^{\dagger}_{\mathbf{r},+,\uparrow}, c^{\dagger}_{\mathbf{r},+,\downarrow}, c^{\dagger}_{\mathbf{r},-,\uparrow}, c^{\dagger}_{\mathbf{r},-,\downarrow})$ with $\pm$ denoting the parity of the basis and $\uparrow/\downarrow$ the spin. The function $f(\mathbf{r})$ equals 1 for several layers close to one termination and 0 for all other layers. $g_{1i} \pm g_{2i}$ are the g-factors for the two respective orbits. B_i is the magnetic field along i-th direction. The surface state at one termination is gapped due to the Zeeman effect, leaving only one gapless state as shown in Fig. 3c, e. Although there is a warping effect on the gapless Dirac cone at the [001] termination compared to the [100] termination, the Hall conductivity remains quantized at $-e^2/2h$ when the chemical potential intersects only the gapless Dirac cone, as shown in Fig. 3d, f[35]. This quantization persists due to the maintenance of local time-reversal symmetry. For the [001] termination, the application of an in-plane Zeeman field along x direction which breaks the local time-reversal symmetry but maintains mirror symmetry σ_v, such that the Hall conductivity will still be half-quantized according to our theory.

Topological crystalline insulator SnTe. The compound SnTe is known to crystallize in the rock-salt structure, which has the space group Fm-3m or No. 225[64,65]. The space group Fm-3m is one of the cubic space groups and part of the face-centered cubic (fcc) Bravais lattice. The generators for the space group Fm-3m typically include: (i) four-fold rotation (C_4) about the [001] axis, (ii) threefold rotation (C_3) about the [111] diagonal, (iii) inversion (I), (iv) translation by one half of the unit cell along the face diagonal. SnTe also exhibits time-reversal symmetry. The combination of these symmetry operations generates the entire set of operations for the Fm-3m space group. Figure 4a displays the 3D Brillouin zone of the rock-salt crystal structure. Crystals of the SnTe class possess small direct band gaps at four symmetry-related time-reversal invariant momenta (TRIMs), specifically at the L points (i.e., L_1, L_2, L_3 and L_4 in Fig. 4a). The topological character of the crystal is defined by a mirror Chern number $N_M = (N_{+i} - N_{-i})/2$ associated with the plane passing through Γ and L_3, L_4 points. N_M can be tuned via the model parameter m, which represents the on-site potential difference between Sn and Te. Here, $N_{\pm i}$ denote the Chern numbers of the Bloch eigenstates with mirror eigenvalues of $\pm i$, respectively. The value of N_M transitions from -2 to 0 as m increased, crossing a critical value $m_c \simeq 2.06$eV. Correspondingly, the 3D band structure along high symmetry lines exhibits a band inversion when

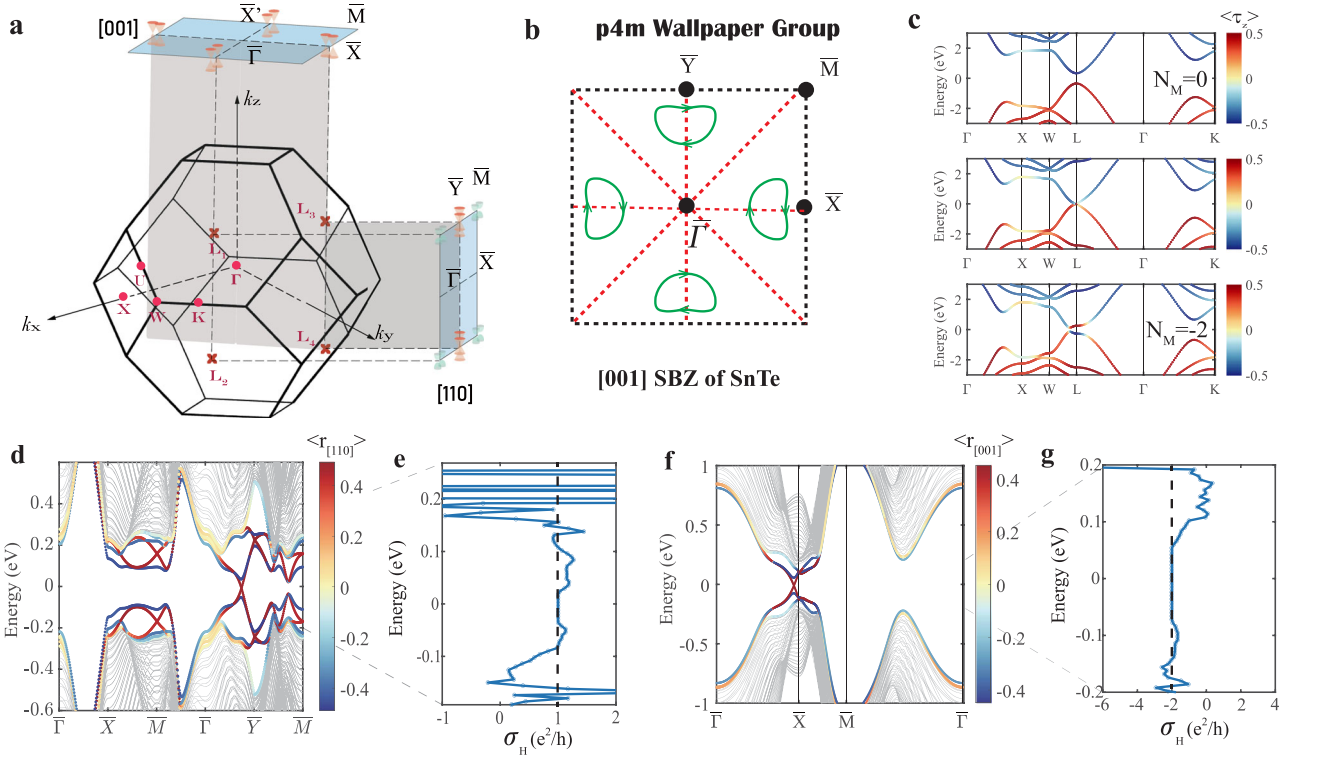

Fig. 4 | The half-quantized Hall phase in topological crystalline insulator. **a** Illustration of high-symmetry points within the 3D Brillouin zone, the projected surface Brillouin zones for the [110] and [001] surfaces of the rock-salt crystal structure, and the locations of Dirac surface states for two terminations. **b** The surface Brillouin zone (SBZ) for the [001] termination. The lines and symbols has the same meaning as Fig. 3b. **c** The 3D band structure along high-symmetry paths for $m > m_c$ ($N_M = 0$), $m = m_c$ (critical point), and $m < m_c$ ($N_M = -2$) with color transition from blue to red representing the population of the wave function at Sn or Te atoms, which can be determined by calculating the expectation value of the orbital polarization operator τ_z. Panels **d** and **e** depict the slab band structure along high symmetry line and Hall conductivity σ_H as a function of chemical potential μ for the [110] termination with a time-reversal symmetry breaking term added on one surface ($\langle r_{[110]} \rangle \sim -0.5$), respectively, while panels **f** and **g** show same results for the [001] termination with a time-reversal symmetry breaking term added on one surface ($\langle r_{[001]} \rangle \sim -0.5$). Parameters: $t_1 = -0.5$, $t_2 = 0.5$, $t_{12} = 0.9$ $\lambda_1 = \lambda_2 = -0.3$, $m = 1.3$ (except for **b**), $\Delta = 0.12$ for **d**, **e**, **f** and **g**; all values are in *eV*.

m surpasses m_c as demonstrated in Fig. 4c. For a nonzero mirror Chern number case, depending on the surface orientation [001] or [110], there are two types of TCI surface states with qualitatively different electronic properties as schematically shown in Fig. 4a. The 2D surface for a [001] termination belongs to wallpaper group $p4m$, and the surface Brillouin zone contains four Dirac cones, resulting in multiple-ring structure in the Fermi loop as illustrated in Fig. 4b. The existence of two gapless Dirac cones along $\bar{\Gamma} - \bar{X}(\bar{\Gamma} - \bar{X}')$ is ensured by the nonzero mirror Chern number associated with the $\Gamma L_3 L_4 (\Gamma L_1 L_2)$ plane, as highlighted by the brown-colored surface in Fig. 4a. The neighboring Dirac cones located near the $\bar{X}$ ($\bar{Y}$) points are time-reversal counterparts, and under time-reversal transformation, the integration loop over one Dirac cone is mapped to the other without altering its orientation. Meanwhile, for a mirror symmetry transformation (along the x-axis), the integration loop over one pair of Dirac cones remains unchanged, while the other pair is interchanged; more importantly, the orientation of the integration is reversed. Conversely, on [110] surface termination, there are only two gapless Dirac cones along along $\bar{\Gamma} - \bar{Y}$, attributable to the presence of a single nonzero mirror Chern number ($|N_M| = 2$) associated with it.

Considering a slab geometry with two distinct terminations, we introduced a time-reversal symmetry-breaking term on one termination, described by the Hamiltonian

$$\mathcal{H}' = \Delta \sum_j (-1)^j \sum_{\mathbf{r},\alpha,\beta} f(\mathbf{r})(\boldsymbol{\sigma} \cdot \mathbf{R}_t)_{\alpha\beta} \mathbf{c}^\dagger_{j\alpha}(\mathbf{r}) \cdot \mathbf{c}_{j\beta}(\mathbf{r}), \tag{12}$$

where $\mathbf{R}_t = (0, 0, 1)$ or $\frac{1}{\sqrt{2}}(1, 1, 0)$ corresponds to the two different terminations, Δ represents the staggered Zeeman field. Figure 4d, f illustrate that while the Dirac cones on the bottom surface exhibit a band gap (indicated by blue), the Dirac cones on the top surface remain gapless which retains the local time-reversal symmetry (signified by red). The number of Dirac cones at the [001] termination is twice that at the [100] termination. Consequently, if the chemical potential intersects only these gapless surface states, the Hall conductivity is quantized at $+e^2/h$ for [110] termination and $-2e^2/h$ for [001] terminations depicted in Fig. 4e, g.

Extrinsic anomalous Hall conductivity

According to Kubo-Streda formula[47,48], the Hall conductivity σ_{xy} can be decomposed into $\sigma_{xy} = \sigma^{\mathrm{I}}_{xy} + \sigma^{\mathrm{II}}_{xy}$. σ^{I}_{xy} and $\sigma^{\mathrm{II}}_{xy}$ are frequently referred to as the Fermi surface and Fermi sea terms, respectively. As the chemical potential is located within the band, σ^{I}_{xy} may also contribute. We now turn our attention to the extrinsic contributions to the anomalous Hall effect, focusing on mechanisms such as skew scattering and side-jump[49,90,91], which primarily arise from σ^{I}_{xy}. Given that the extrinsic contribution primarily arises from states on the Fermi surface, our analysis will be centered on the surface state Hamiltonian in Eq. (9). The side-jump contribution (Fig. 5a, b) to the Hall conductivity can be expressed as follows:

$$\sigma^{sj(a)}_{xy} = \frac{e^2\hbar}{\pi} \int_{\mathbf{k},\mathbf{k}'} \mathrm{Re}[\langle U^{++}_{\mathbf{k}\mathbf{k}'} U^{-+}_{\mathbf{k}'\mathbf{k}} \rangle G^R_{\mathbf{k}+} \gamma^{++}_x(\mathbf{k}) G^A_{\mathbf{k}+} G^R_{\mathbf{k}'+} v^{+-}_y(\mathbf{k}') G^A_{\mathbf{k}'-}], \tag{13}$$

$$\sigma^{sj(b)}_{xy} = \frac{e^2\hbar}{\pi} \int_{\mathbf{k},\mathbf{k}'} \mathrm{Re}[\langle U^{++}_{\mathbf{k}\mathbf{k}'} U^{+-}_{\mathbf{k}'\mathbf{k}} \rangle \gamma^{++}_x(\mathbf{k}) G^R_{\mathbf{k}+} G^R_{\mathbf{k}'+} G^R_{\mathbf{k},-} v^{-+}_y(\mathbf{k}) G^A_{\mathbf{k},+}]. \tag{14}$$

The integral over the momentum space is concisely denoted by $\int_{\mathbf{k}} = \int \frac{d^2\mathbf{k}}{(2\pi)^2}$. $\langle U^{ss'}_{\mathbf{k}\mathbf{k}'} U^{r'r}_{\mathbf{k}'\mathbf{k}} \rangle$ represents the disorder-averaged scattering potential matrix

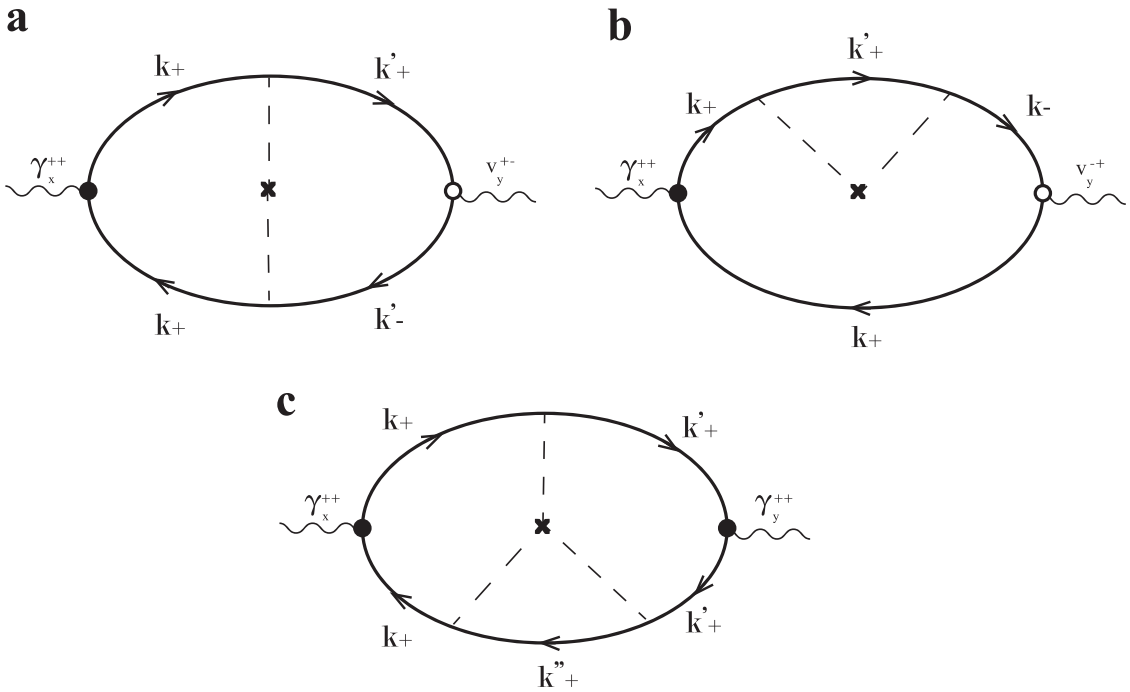

Fig. 5 | Diagrammatic representation of extrinsic contributions to the anomalous Hall effect. a, b Diagrams illustrating side jump contributions. **c** Diagrams depicting skew scattering contributions. The '+' and '-' symbols denote the upper and lower bands, respectively. Dashed lines represent impurity interactions. Empty circles indicate bare current vertices, while filled circles represent renormalized current vertices.

elements where r, s, r', s' are band indices. $G^{R/A}_{\mathbf{k}s} = (\mu - \epsilon^s_{\mathbf{k}} \pm i\eta)^{-1}$ denotes the retarded/advanced Green's function for band s, where $\epsilon^s_{\mathbf{k}}$ denotes the corresponding energy and η is the broadening induced by disorder. $v_y^{ss'}(\mathbf{k})$ and $\gamma_\alpha^{ss'}(\mathbf{k})$ are the velocity matrix element and remonetized velocity matrix element with vertex correction, respectively.

Considering a system with time reversal symmetry, we have $\epsilon^s_{\mathbf{k}} = \epsilon^s_{-\mathbf{k}}$ with $s = \pm$, $v_\alpha^{ss'}(\mathbf{k}) = -v_\alpha^{s's}(-\mathbf{k})$ and $U^{ss'}_{\mathbf{k}\mathbf{k}'} = U^{s's}_{-\mathbf{k}',-\mathbf{k}}$. These symmetries lead to the following relations for the side-jump contributions to the Hall conductivity:

$$\sigma_{xy}^{sj(a)} = \frac{e^2\hbar}{\pi}\int_{\mathbf{k},\mathbf{k}'} \mathrm{Re}[\langle U^{++}_{\mathbf{k}\mathbf{k}'} U^{-+}_{\mathbf{k}'\mathbf{k}}\rangle \gamma_x^{++}(\mathbf{k}) v_y^{+-}(\mathbf{k}')] G^R_{\mathbf{k}+} G^A_{\mathbf{k}+} \mathrm{Re}[G^R_{\mathbf{k}'+} G^A_{\mathbf{k}'-}], \quad (15)$$

$$\sigma_{xy}^{sj(b)} = \frac{e^2\hbar}{\pi}\int_{\mathbf{k},\mathbf{k}'} \mathrm{Re}[\langle U^{++}_{\mathbf{k}\mathbf{k}'} U^{+-}_{\mathbf{k}'\mathbf{k}}\rangle \gamma_x^{++}(\mathbf{k}) v_y^{-+}(\mathbf{k})] G^R_{\mathbf{k}+} G^A_{\mathbf{k},+} \mathrm{Re}[G^R_{\mathbf{k}'+} G^R_{\mathbf{k},-}]. \quad (16)$$

For a generic surface state Hamiltonian in Eq. (9), the term involving scattering potentials and velocities can be expressed as $\mathrm{Re}[\langle U^{++}_{\mathbf{k}\mathbf{k}'} U^{-+}_{\mathbf{k}'\mathbf{k}}\rangle \gamma_x^{++}(\mathbf{k}) v_y^{+-}(\mathbf{k}')] \propto \sin(\theta)\sin(\phi)\{\cos(\theta')\cos(\phi')[\sin(\theta)\cos(\theta')\cos(\phi-\phi') - \cos(\theta)\sin(\theta')] - \sin(\theta)\sin(\phi')\sin(\phi-\phi')\}$ with $\cos\theta = \frac{g(\mathbf{k})}{\mu}$ and $\phi = \mathrm{Arg}[f(\mathbf{k})]$. For systems possessing 3-fold, 4-fold or 6-fold rotational symmetry, the side-jump contributions $\sigma_{xy}^{sj(a)} = \sigma_{xy}^{sj(b)} = 0$ are zero after summing over points related by symmetry, such as $\mathbf{k}, D_n\mathbf{k}, \ldots, D_n^{n-1}\mathbf{k}$. In system with 2-fold rotational symmetry, these contributions cannot be directly ruled out by symmetry analysis alone. However, considering the nature of $\mathrm{Re}[G^R_{\mathbf{k}'+} G^A_{\mathbf{k}'-}] \simeq \frac{\mu-\epsilon_{\mathbf{k}'}}{2\mu(\eta^2+(\epsilon_{\mathbf{k}'}-\mu)^2)}$, it becomes apparent that states slightly above and below the Fermi surface dominate the contribution, but with opposite signs. Therefore, in this situation, the side-jump contribution σ_{xy}^{sj} is vanishingly small.

Skew scattering contributions arise from the asymmetric part of the scattering rates in higher-order scattering processes. The leading contribution is associated with the third-order disorder correlation and inversely depends on the impurity concentration n shown diagrammatically as Fig. 5c. The skew scattering conductivity σ_{xy}^{sk} can be written as:

$$\sigma_{xy}^{sk} = \frac{e^2\hbar}{\pi}\int_{\mathbf{k},\mathbf{k}',\mathbf{k}''} \mathrm{Re}[\langle U^{++}_{\mathbf{k}\mathbf{k}'} U^{++}_{\mathbf{k}'\mathbf{k}''} U^{++}_{\mathbf{k}''\mathbf{k}}\rangle G^A_{\mathbf{k}+} \gamma_x^{++}(\mathbf{k}) G^R_{\mathbf{k},+} G^R_{\mathbf{k}'+} \gamma_y^{++}(\mathbf{k}') G^A_{\mathbf{k}'+} G^A_{\mathbf{k}''+}]. \quad (17)$$

By using time-reversal symmetry, the expression simplifies further as:

$$\sigma_{xy}^{sk} = \frac{e^2\hbar}{\pi}\int_{\mathbf{k},\mathbf{k}',\mathbf{k}''} \mathrm{Re}[\langle U^{++}_{\mathbf{k}\mathbf{k}'} U^{++}_{\mathbf{k}'\mathbf{k}''} U^{++}_{\mathbf{k}''\mathbf{k}}\rangle \gamma_x^{++}(\mathbf{k}) \gamma_y^{++}(\mathbf{k}')] G^A_{\mathbf{k}+} G^R_{\mathbf{k},+} G^R_{\mathbf{k}'+} G^A_{\mathbf{k}'+} \mathrm{Re}[G^A_{\mathbf{k}''+}]. \quad (18)$$

For systems with 3-fold, 4-fold or 6-fold rotational symmetry, σ_{xy}^{sk} is shown to be zero after summing contributions from symmetry-related points. In systems with 2-fold rotational symmetry, the skew scattering contribution σ_{xy}^{sk} is similarly small due to the factor $\mathrm{Re}\left[G^A_{\mathbf{k}''+}\right] \simeq \frac{\mu-\epsilon_{\mathbf{k}''}}{\eta^2+(\epsilon_{\mathbf{k}''}-\mu)^2}$.

In conclusion, the extrinsic contributions to the Hall conductivity in quantum anomalous Hall metals are negligible for systems with rotational symmetry and time reversal symmetry.

Discussion

To conclude, we proposed the $\mathbb{Z}/2$ topological invariant to characterize the metallic nature and half quantized Hall conductivity of topological metals out of an ordinary metallic ferromagnet. Local symmetry near the Fermi surface safeguards the quantization of the Hall conductivity. The local symmetry may emerge in the magnetic structures of topological materials by means of the locality of the surface states. We have identified two distinct categories of local unitary and anti-unitary symmetries in proximity to the Fermi surface of electron states. Numerical calculation provides substantial evidence to support the existence of the plateau of the half-quantized Hall conductivity in semi-magnetic heterostructure of topological insulator Bi_2Te_3 and Bi_2Se_3 film for $\nu = 1$ and topological crystalline insulator SnTe films for $\nu = 2$ and 4.

Method

Proof of Eq. 3 for the multi-band case

The can be generalized into multi-bands case. We have assumed that each band is isolated, meaning it remains separated by a finite energy gap from both the adjacent lower and higher bands throughout the entire Brillouin zone. However, in real crystals, the valence bands may become degenerate at certain points or lines within the Brillouin zone due to either symmetry or accidental degeneracy. Consequently, the Bloch functions for energy eigenstates, often exhibit singularities as a function of $\mathbf{k}$ near these degeneracies. To address this situation, it is generally useful to define an isolated group of J bands to be a set of J consecutive energy bands that do not become degenerate with any lower or higher band anywhere in the Brillouin zone. The multi-band Berry connection and curvature for such a system are given by: $\mathbf{A}^{mn}(\mathbf{k}) = i\langle u_{m\mathbf{k}}|\partial_{\mathbf{k}}|u_{n\mathbf{k}}\rangle$ and $\Omega^{mn}_{xy}(\mathbf{k}) = \partial_{k_x}A^{mn}_y(\mathbf{k}) - \partial_{k_y}A^{mn}_x(\mathbf{k}) + i[A_x(\mathbf{k}), A_y(\mathbf{k})]^{mn}$. The trace of these two quantities satisfies the same version of Stokes' theorem as the single-band case. The Hall conductivity resulting from the J bands can be calculated as $\sigma^J_{xy} = \frac{e^2}{\hbar}\sum_{n=1}^{J}\int_{\mathrm{BZ}}\frac{d^2\mathbf{k}}{(2\pi)^2}f_n(\mathbf{k})\Omega^{nn}_{xy}(\mathbf{k})$. In particular, if we assume the Fermi energy intersects a single band $n = 1$, and the other $J-1$ bands are fully occupied, we can divide the Brillouin zone into two subregions S^1 and S^2: S^1 is the inner region enclosing by the Fermi surface loop, where metallic band is well separated from all others ; $\mathrm{S}^2 = \mathrm{BZ} - \mathrm{S}^1$, the bands may experience degeneracies. Since the contribution comes solely from the occupied states, the Hall conductivity can be reformulated as an areal integral over these two subregions:

$$\sigma^J_{xy} = \frac{e^2}{2\pi\hbar}\left(\int_{\mathrm{S}^1} d\mathbf{k}\Omega^{\mathrm{tr}'}_{xy}(\mathbf{k}) + \int_{\mathrm{S}^2} d\mathbf{k}\Omega^{\mathrm{tr}}_{xy}(\mathbf{k})\right) \tag{19}$$

where $\Omega^{\mathrm{tr}}_{xy}(\mathbf{k}) = \sum_{n=1}^{J}\Omega^{nn}_{xy}(\mathbf{k})$ represents the trace over all J bands, and $\Omega^{\mathrm{tr}'}_{xy}(\mathbf{k}) = \sum_{n=2}^{J}\Omega^{nn}_{xy}(\mathbf{k})$ excludes the band intersecting the Fermi surface. By applying the Stokes' theorem, the Hall conductivity can be expressed as:

$$\sigma^J_{xy} = \frac{e^2}{2\pi h}\left(\int_{\mathrm{C}^1} d\mathbf{l}\cdot\mathbf{A}^{\mathrm{tr}}(\mathbf{k}) + \int_{\mathrm{C}^2} d\mathbf{l}\cdot\mathbf{A}^{\mathrm{tr}'}(\mathbf{k})\right) \tag{20}$$

where $\mathbf{A}^{\mathrm{tr}}(\mathbf{k}) = \sum_{n=1}^{J}\mathbf{A}^{nn}(\mathbf{k})$ and $\mathbf{A}^{\mathrm{tr}'} = \sum_{n=2}^{J}\mathbf{A}^{nn}(\mathbf{k})$. Along C^1, where the metallic band is non-degenerate with the others, we can express the trace of the Berry connection as $\mathbf{A}^{\mathrm{tr}}(\mathbf{k}) = \mathbf{A}^{\mathrm{tr}'}(\mathbf{k}) + \mathbf{A}^{11}(\mathbf{k})$. Considering C^1 and C^2 are oriented in opposite directions, the Hall conductivity is given by

$$\sigma^J_{xy} = \frac{e^2}{2\pi h}\int_{\mathrm{C}_\mu} d\mathbf{l}\cdot\mathbf{A}^{11}(\mathbf{k}). \tag{21}$$

This equation summarizes the contribution to the Hall conductivity from an isolated group of J bands, considering the particular case where the Fermi energy crosses only one band, and the remaining $J-1$ bands are fully occupied.

The surface states classification procedure

The classification of the minimal 2×2 matrix of surface state Hamiltonian $H(\mathbf{k})$ can be performed as follows. We consider the symmetry constraints imposed on $H(\mathbf{k})$ in the presence of T and C_{nz}:

$$TH(\mathbf{k})T^{-1} = H(-\mathbf{k}), \tag{22}$$

$$C_{nz}H(\mathbf{k})C^{-1}_{nz} = H(D_{nz}\mathbf{k}). \tag{23}$$

Here, n is restricted to be 2, 3, 4, 6 in periodic lattice systems. Let us first consider surface states in the vicinity of a high symmetry point invariant under C_{nz} and time reversal operations, such as $\bar{\Gamma}$ and $\bar{M}$-points. Since we are interested in the form of gapless structures at $\mathbf{k}\simeq 0$, we expand f and g to leading order in $\mathbf{k}$[92],

$$f(k_+,k_-) = vk_+^pk_-^q, g(k_+,k_-) = v'k_+^rk_-^s + H.c. \tag{24}$$

where $v, v'\in\mathbb{C}$ and p, q, r, s are non-negative integers, $k_\pm = k_x \pm ik_y$.

If $g(\mathbf{k}) = 0$, the Hamiltonian for the surface states contains only two Dirac matrices, expressed as $H(\mathbf{k}) = f(\mathbf{k})\sigma_+ + f^*(\mathbf{k})\sigma_-$. Owing to an additional chiral (sub-lattice) symmetry $\{\mathcal{S}, H(\mathbf{k})\} = 0$ with $\mathcal{S} = -\sigma_z$, we can define the $\mathbb{Z}$-valued topological number W_1 along a loop C[8,9], $w = \frac{1}{4\pi i}\oint_C d\mathbf{k}\cdot\mathrm{Tr}[\mathcal{S}H^{-1}(\mathbf{k})\nabla_{\mathbf{k}}H(\mathbf{k})]$. By substituting the Hamiltonian, the winding number reduced to $w = \frac{1}{2\pi}\oint_C d\mathbf{k}\cdot\nabla_{\mathbf{k}}\mathrm{Arg}[f(\mathbf{k})]$. Let D_i be a disk enclosing an ith Dirac point, so the total winding number is

$$w = \frac{1}{2\pi}\oint_{\cup_i\partial D_i} d\mathbf{k}\cdot\nabla_{\mathbf{k}}\mathrm{Arg}[f(\mathbf{k})] \tag{25}$$

with ∂D_i as the boundary of D_i. If $f(\mathbf{k}) = v_+k_+^n + v_-k_-^n$, the winding number $w = -n$ for $|v_+| > |v_-|$ and $w = +n$ for $|v_+| < |v_-|$.

(i) For spin 1/2 system, T operator can be represented as $T = i\sigma_yK$ with $T^2 = -1$, where $\sigma_{x,y,z}$ are Pauli matrices for spin degrees of freedom and K stands for complex conjugation. The invariance of the Hamiltonian under TR in Eq. (22) leads to the relations: $f(-\mathbf{k}) = -f(\mathbf{k})$ and $g^*(-\mathbf{k}) = -g(\mathbf{k})$. Thus, both f and g are odd functions of $\mathbf{k}$. When $D_{nz}\mathbf{k} = \mathbf{k}$ is satisfied, we have $[C_{nz}, H(\mathbf{k})] = 0$. Using a basis in which C_{nz} is diagonal, C_{nz} can be represented by a diagonal matrix $C_{nz} = diag[\alpha_l, \alpha_m]$, where $\alpha_l = \exp(i\frac{2\pi}{n}(l+\frac{1}{2}))$ with $l = 0, 1, \ldots, n-1$. For convenience, we can express C_{nz} as $C_{nz} = e^{i\pi(\frac{1+l+m}{n}+\frac{l-m}{n}\sigma_z)}$. We assume the commutation relation $[C_{nz}, T] = 0$, so that the representation of the C_{nz} operator is restricted to $C_{nz} = e^{i\pi(\frac{2l+1}{n}\sigma_z)}$. From Eq. (23), we have

$$\begin{aligned} e^{i2\pi(2l+1)/n}f(e^{i2\pi/n}k_+, e^{-i2\pi/n}k_- = f(k_+,k_-),\\ g(e^{i2\pi/n}k_+, e^{-i2\pi/n}k_-) = g(k_+,k_-). \end{aligned} \tag{26}$$

Substituting Eq. (24) into Eqs. (26) yields the relations:

$$e^{i2\pi(2l+1+p-q)/n} = 1, e^{i2\pi(r-s)/n} = 1 \tag{27}$$

which gives

$$\begin{aligned} q - p &= 2l+1, \mathrm{mod}\ n,\\ r - s &= 0, \mathrm{mod}\ n. \end{aligned} \tag{28}$$

For $n = 2, 4, 6$, since $g(k_+, k_-)$ is odd function, we find $g(\mathbf{k}) = 0$. For $n = 3$, the lowest order non-vanishing term for g can be expressed as

$$g(k_+,k_-) = v'k_+^3 + v'^*k_-^3. \tag{29}$$

(ii) For spinless system, T operator can be represented by the operator $T = \sigma_xK$ with $T^2 = +1$, where $\sigma_{x,y,z}$ are Pauli matrices for pseudo-spin basis and K stands for complex conjugation. The invariance of the Hamiltonian under TR as stated in Eq. (22) leads to the relations: $f(-\mathbf{k}) = f(\mathbf{k})$ and $g^*(-\mathbf{k}) = -g(\mathbf{k})$. Thus, f and g are even and odd functions of $\mathbf{k}$, respectively. When $D_{nz}\mathbf{k} = \mathbf{k}$ is satisfied, $[C_{nz}, H(\mathbf{k})] = 0$. In a basis characterized by orbital angular momentum l and m, C_{nz} can be represented by a diagonal matrix $C_{nz} = diag[\alpha_l, \alpha_m]$, where $\alpha_l = \exp(i\frac{2\pi}{n}l)$ with $l = 0, 1, \ldots, n-1$. This can be expressed as $C_{nz} = e^{i\pi(\frac{l+m}{n}+\frac{l-m}{n}\sigma_z)}$. Assuming the commutation relation $[C_{nz}, T] = 0$, so that the representation of the C_{nz} operator is restricted to $C_{nz} = e^{i\frac{2\pi l}{n}\sigma_z}$. From Eq. (23), we have

$$\begin{aligned} e^{i\frac{4\pi l}{n}}f(e^{i2\pi/n}k_+, e^{-i2\pi/n}k_-) = f(k_+,k_-),\\ g(e^{i2\pi/n}k_+, e^{-i2\pi/n}k_-) = g(k_+,k_-) \end{aligned} \tag{30}$$

From Eq. (24), we have

$$e^{i\frac{2\pi}{n}(2l+p-q)} = 1, e^{i\frac{2\pi}{n}(r-s)} = 1 \tag{31}$$

resulting in the conditions:

$$\begin{aligned} q - p &= 2l, \mathrm{mod}\ n \\ r - s &= 0, \mathrm{mod}\ n. \end{aligned} \tag{32}$$

For $g(\mathbf{k})$, the symmetry constraints are the same as those for the spin-1/2 system. When $\mathrm{mod}(2l, n) = 0$, the leading term of $f(\mathbf{k})$ is a constant. When $\mathrm{mod}(2l, n) \neq 0$, the leading term of $f(\mathbf{k})$ is in $|\mathbf{k}|^2$.

Tight-binding model of SnTe

The tight-binding model of SnTe is constructed from the Wannier functions of the conduction and valence bands, which are primarily three p-orbitals of Sn and Te atoms. The tight-binding Hamiltonian $\mathcal{H}_{\mathrm{SnTe}}$ is given by[64]

$$\begin{aligned} \mathcal{H}_{\mathrm{SnTe}} = & \ m\sum_j (-1)^j \sum_{\mathbf{r},\alpha} \mathbf{c}^\dagger_{j\alpha}(\mathbf{r}) \cdot \mathbf{c}_{j\alpha}(\mathbf{r}) \\ & + \sum_{j,j'} t_{jj'} \sum_{(\mathbf{r},\mathbf{r}'),\alpha} \mathbf{c}^\dagger_{j\alpha}(\mathbf{r}) \cdot \hat{\mathbf{d}}_{\mathbf{r}\mathbf{r}'} \hat{\mathbf{d}}_{\mathbf{r}\mathbf{r}'} \cdot \mathbf{c}_{j'\alpha}(\mathbf{r}') + h.c. \\ & + \sum_j i\lambda_j \sum_{\mathbf{r},\alpha,\beta} \mathbf{c}^\dagger_{j\alpha}(\mathbf{r}) \times \mathbf{c}_{j\beta}(\mathbf{r}) \cdot \boldsymbol{\sigma}_{\alpha\beta} \end{aligned} \tag{33}$$

Here $\mathbf{r}$ represents the lattice site, while $j = 1, 2$ distinguishes between Sn and Te atoms. The spin of the electrons is denoted by $\alpha = \uparrow, \downarrow$. The creation operator vector $\mathbf{c}^\dagger$ and the annihilation operator vector $\mathbf{c}$ correspond to the three p-orbitals. The parameter m indicates the on-site potential difference between Sn and Te. The hopping amplitude between nearest-neighbor Sn and Te is symmetric, with $t_{12} = t_{21}$. The parameters t_{11} and t_{22} characterize the next nearest-neighbor hopping amplitudes within the same sublattice. The unit vector $\hat{\mathbf{d}}_{\mathbf{r}\mathbf{r}'} = \frac{\mathbf{r}-\mathbf{r}'}{|\mathbf{r}-\mathbf{r}'|}$ connects sites $\mathbf{r}$ and $\mathbf{r}'$. The terms λ_1 and λ_2 represent the spin-orbit couplings for the two types of atoms. The bulk and surface bands of the tight-binding Hamiltonian accurately reproduce the essential features of the first-principles calculations.

Data availability

All data generated or analysed during this study are included in this published article (and its Supplementary Information files).

Received: 16 August 2024; Accepted: 20 December 2024;
Published online: 02 January 2025

References

1. Schnyder, A. P., Ryu, S., Furusaki, A. & Ludwig, A. W. Classification of topological insulators and superconductors in three spatial dimensions. *Phys. Rev. B* **78**, 195125 (2008).
2. Kitaev, A. *Periodic table for topological insulators and superconductors*, 1134, 22–30 (American Institute of Physics, 2009).
3. Ryu, S., Schnyder, A. P., Furusaki, A. & Ludwig, A. W. W. Topological insulators and superconductors: tenfold way and dimensional hierarchy. *N. J. Phys.* **12**, 065010 (2010).
4. Morimoto, T. & Furusaki, A. Topological classification with additional symmetries from clifford algebras. *Phys. Rev. B* **88**, 125129 (2013).
5. Zhao, Y. & Wang, Z. Topological classification and stability of fermi surfaces. *Phys. Rev. Lett.* **110**, 240404 (2013).
6. Matsuura, S., Chang, P.-Y., Schnyder, A. P. & Ryu, S. Protected boundary states in gapless topological phases. *N. J. Phys.* **15**, 065001 (2013).
7. Shiozaki, K. & Sato, M. Topology of crystalline insulators and superconductors. *Phys. Rev. B* **90**, 165114 (2014).
8. Chiu, C.-K. & Schnyder, A. P. Classification of reflection-symmetry-protected topological semimetals and nodal superconductors. *Phys. Rev. B* **90**, 205136 (2014).
9. Chiu, C.-K., Teo, J. C. Y., Schnyder, A. P. & Ryu, S. Classification of topological quantum matter with symmetries. *Rev. Mod. Phys.* **88**, 035005 (2016).
10. Hasan, M. Z. & Kane, C. L. Colloquium: Topological insulators. *Rev. Mod. Phys.* **82**, 3045–3067 (2010).
11. Qi, X.-L. & Zhang, S.-C. Topological insulators and superconductors. *Rev. Mod. Phys.* **83**, 1057–1110 (2011).
12. Shen, S.-Q. *Topological Insulators: Dirac Equation in Condensed Matter* 2nd edn (Springer, Singapore, 2017). https://doi.org/10.1007/978-981-10-4606-3_2.
13. Thouless, D. J., Kohmoto, M., Nightingale, M. P. & den Nijs, M. Quantized hall conductance in a two-dimensional periodic potential. *Phys. Rev. Lett.* **49**, 405–408 (1982).
14. Niu, Q., Thouless, D. J. & Wu, Y.-S. Quantized hall conductance as a topological invariant. *Phys. Rev. B* **31**, 3372–3377 (1985).
15. Simon, B. Holonomy, the quantum adiabatic theorem, and berry's phase. *Phys. Rev. Lett.* **51**, 2167–2170 (1983).
16. Hatsugai, Y. Chern number and edge states in the integer quantum hall effect. *Phys. Rev. Lett.* **71**, 3697–3700 (1993).
17. Haldane, F. D. M. Model for a quantum hall effect without landau levels: Condensed-matter realization of the "parity anomaly". *Phys. Rev. Lett.* **61**, 2015–2018 (1988).
18. Yu, R. et al. Quantized anomalous hall effect in magnetic topological insulators. *Science* **329**, 61–64 (2010).
19. Chu, R.-L., Shi, J. & Shen, S.-Q. Surface edge state and half-quantized hall conductance in topological insulators. *Phys. Rev. B* **84**, 085312 (2011).
20. Chang, C.-Z. et al. Experimental observation of the quantum anomalous hall effect in a magnetic topological insulator. *Science* **340**, 167–170 (2013).
21. Checkelsky, J. G. et al. Trajectory of the anomalous hall effect towards the quantized state in a ferromagnetic topological insulator. *Nat. Phys.* **10**, 731–736 (2014).
22. Kane, C. L. & Mele, E. J. Z_2 topological order and the quantum spin hall effect. *Phys. Rev. Lett.* **95**, 146802 (2005).
23. Bernevig, B. A., Hughes, T. L. & Zhang, S.-C. Quantum spin hall effect and topological phase transition in HgTe quantum wells. *Science* **314**, 1757–1761 (2006).
24. Slager, R.-J., Mesaros, A., Juričić, V. & Zaanen, J. The space group classification of topological band-insulators. *Nat. Phys.* **9**, 98–102 (2013).
25. Kruthoff, J., de Boer, J., van Wezel, J., Kane, C. L. & Slager, R.-J. Topological classification of crystalline insulators through band structure combinatorics. *Phys. Rev. X* **7**, 041069 (2017).
26. Shiozaki, K., Sato, M. & Gomi, K. Topological crystalline materials: General formulation, module structure, and wallpaper groups. *Phys. Rev. B* **95**, 235425 (2017).
27. Song, Z., Zhang, T., Fang, Z. & Fang, C. Quantitative mappings between symmetry and topology in solids. *Nat. Commun.* **9**, 3530 (2018).
28. Khalaf, E., Po, H. C., Vishwanath, A. & Watanabe, H. Symmetry indicators and anomalous surface states of topological crystalline insulators. *Phys. Rev. X* **8**, 031070 (2018).
29. Song, Z., Huang, S.-J., Qi, Y., Fang, C. & Hermele, M. Topological states from topological crystals. *Sci. Adv.* **5**, eaax2007 (2019).
30. Elcoro, L. et al. Magnetic topological quantum chemistry. *Nat. Commun.* **12**, 5965 (2021).
31. Haldane, F. D. M. Berry curvature on the fermi surface: Anomalous hall effect as a topological fermi-liquid property. *Phys. Rev. Lett.* **93**, 206602 (2004).
32. Fu, B., Zou, J.-Y., Hu, Z.-A., Wang, H.-W. & Shen, S.-Q. Quantum anomalous semimetals. *npj Quantum Mater.* **7**, 94 (2022).
33. Mogi, M. et al. Experimental signature of the parity anomaly in a semi-magnetic topological insulator. *Nat. Phys.* **18**, 390–394 (2022).

34. Zou, J.-Y., Fu, B., Wang, H.-W., Hu, Z.-A. & Shen, S.-Q. Half-quantized hall effect and power law decay of edge-current distribution. *Phys. Rev. B* **105**, L201106 (2022).
35. Zou, J.-Y. et al. Half-quantized hall effect at the parity-invariant fermi surface. *Phys. Rev. B* **107**, 125153 (2023).
36. Gong, M., Liu, H., Jiang, H., Chen, C.-Z. & Xie, X. Half-quantized helical hinge currents in axion insulators. *Natl Sci. Rev.* **10**, nwad025 (2023).
37. Yang, H., Song, L., Cao, Y. & Yan, P. Realization of wilson fermions in topolectrical circuits. *Commun. Phys.* **6**, 211 (2023).
38. Ning, Z., Ding, X., Xu, D.-H. & Wang, R. Robustness of half-integer quantized hall conductivity against disorder in an anisotropic dirac semimetal with parity anomaly. *Phys. Rev. B* **108**, L041104 (2023).
39. Wang, H.-W., Fu, B. & Shen, S.-Q. Signature of parity anomaly: Crossover from one half to integer quantized hall conductance in a finite magnetic field. *Phys. Rev. B* **109**, 075113 (2024).
40. Wan, Y.-H. & Sun, Q.-F. Quarter-quantized thermal hall effect with parity anomaly. *Phys. Rev. B* **109**, 195408 (2024).
41. Zhou, H., Chen, C.-Z., Sun, Q.-F. & Xie, X. Dissipative chiral channels, ohmic scaling, and half-integer hall conductivity from relativistic quantum hall effect. *Phys. Rev. B* **109**, 115305 (2024).
42. Fu, B., Bai, K.-Z. & Shen, S.-Q. Half-quantum mirror hall effect. *Nat. Commun.* **15**, 6939 (2024).
43. Hutchinson, J. & Le Hur, K. Quantum entangled fractional topology and curvatures. *Commun. Phys.* **4**, 144 (2021).
44. Le Hur, K. One-half topological number in entangled quantum physics. *Phys. Rev. B* **108**, 235144 (2023).
45. del Pozo, F., Herviou, L. & Le Hur, K. Fractional topology in interacting one-dimensional superconductors. *Phys. Rev. B* **107**, 155134 (2023).
46. Le Hur, K. Interacting topological quantum aspects with light and geometrical functions. *Phys. Rep.* **1104**, 1–42 (2025).
47. Kubo, R. Statistical-mechanical theory of irreversible processes. i. general theory and simple applications to magnetic and conduction problems. *J. Phys. Soc. Jpn.* **12**, 570–586 (1957).
48. Streda, P. Theory of quantised hall conductivity in two dimensions. *J. Phys. C: Solid State Phys.* **15**, L717 (1982).
49. Sinitsyn, N., MacDonald, A., Jungwirth, T., Dugaev, V. & Sinova, J. Anomalous hall effect in a two-dimensional dirac band: The link between the kubo-streda formula and the semiclassical boltzmann equation approach. *Phys. Rev. B* **75**, 045315 (2007).
50. Nagaosa, N., Sinova, J., Onoda, S., MacDonald, A. H. & Ong, N. P. Anomalous hall effect. *Rev. Mod. Phys.* **82**, 1539–1592 (2010).
51. Xiao, D., Chang, M.-C. & Niu, Q. Berry phase effects on electronic properties. *Rev. Mod. Phys.* **82**, 1959–2007 (2010).
52. Thouless, D. Wannier functions for magnetic sub-bands. *J. Phys. C: Solid State Phys.* **17**, L325 (1984).
53. Thonhauser, T. & Vanderbilt, D. Insulator/chern-insulator transition in the haldane model. *Phys. Rev. B* **74**, 235111 (2006).
54. Beenakker, C. W. J., Donís Vela, A., Lemut, G., Pacholski, M. J. & Tworzydło, J. Tangent fermions: Dirac or majorana fermions on a lattice without fermion doubling. *Ann. Phys.* **535**, 2300081 (2023).
55. Wigner, E. *Group theory: and its application to the quantum mechanics of atomic spectra* Vol. 5 (Elsevier, 2012).
56. Park, H. et al. Observation of fractionally quantized anomalous hall effect. *Nature* **622**, 74–79 (2023).
57. Lu, Z. et al. Fractional quantum anomalous hall effect in multilayer graphene. *Nature* **626**, 759–764 (2024).
58. Onoda, S., Sugimoto, N. & Nagaosa, N. Intrinsic versus extrinsic anomalous hall effect in ferromagnets. *Phys. Rev. Lett.* **97**, 126602 (2006).
59. Sun, S., Weng, H. & Dai, X. Possible quantization and half-quantization in the anomalous hall effect caused by in-plane magnetic field. *Phys. Rev. B* **106**, L241105 (2022).
60. Fu, L., Kane, C. L. & Mele, E. J. Topological insulators in three dimensions. *Phys. Rev. Lett.* **98**, 106803 (2007).
61. Moore, J. E. & Balents, L. Topological invariants of time-reversal-invariant band structures. *Phys. Rev. B* **75**, 121306 (2007).
62. Fu, L. & Kane, C. L. Topological insulators with inversion symmetry. *Phys. Rev. B* **76**, 045302 (2007).
63. Fu, L. Topological crystalline insulators. *Phys. Rev. Lett.* **106**, 106802 (2011).
64. Hsieh, T. H. et al. Topological crystalline insulators in the snte material class. *Nat. Commun.* **3**, 982 (2012).
65. Ando, Y. & Fu, L. Topological crystalline insulators and topological superconductors: From concepts to materials. *Annu. Rev. Condens. Matter Phys.* **6**, 361–381 (2015).
66. Ahn, J., Park, S. & Yang, B.-J. Failure of nielsen-ninomiya theorem and fragile topology in two-dimensional systems with space-time inversion symmetry: application to twisted bilayer graphene at magic angle. *Phys. Rev. X* **9**, 021013 (2019).
67. Wieder, B. J. et al. Wallpaper fermions and the nonsymmorphic dirac insulator. *Science* **361**, 246–251 (2018).
68. Fang, C. & Fu, L. New classes of topological crystalline insulators having surface rotation anomaly. *Sci. Adv.* **5**, eaat2374 (2019).
69. Zhang, S. et al. Anomalous quantization trajectory and parity anomaly in co cluster decorated bisbtese2 nanodevices. *Nat. Commun.* **8**, 977 (2017).
70. Lu, R. et al. Half-magnetic topological insulator with magnetization-induced dirac gap at a selected surface. *Phys. Rev. X* **11**, 011039 (2021).
71. Bai, K.-Z., Fu, B., Zhang, Z. & Shen, S.-Q. Metallic quantized anomalous hall effect without chiral edge states. *Phys. Rev. B* **108**, L241407 (2023).
72. Mogi, M. et al. A magnetic heterostructure of topological insulators as a candidate for an axion insulator. *Nat. Mater.* **16**, 516–521 (2017).
73. Xiao, D. et al. Realization of the axion insulator state in quantum anomalous hall sandwich heterostructures. *Phys. Rev. Lett.* **120**, 056801 (2018).
74. Zhang, D. et al. Topological axion states in the magnetic insulator $mnbi_2te_4$ with the quantized magnetoelectric effect. *Phys. Rev. Lett.* **122**, 206401 (2019).
75. Chen, R. et al. Using nonlocal surface transport to identify the axion insulator. *Phys. Rev. B* **103**, L241409 (2021).
76. Chen, R., Sun, H.-P. & Zhou, B. Side-surface-mediated hybridization in axion insulators. *Phys. Rev. B* **107**, 125304 (2023).
77. Fu, L. Hexagonal warping effects in the surface states of the topological insulator bi_2te_3. *Phys. Rev. Lett.* **103**, 266801 (2009).
78. Liu, C.-X. et al. Model hamiltonian for topological insulators. *Phys. Rev. B* **82**, 045122 (2010).
79. König, M. et al. Quantum spin hall insulator state in HgTe quantum wells. *Science* **318**, 766–770 (2007).
80. König, M. et al. The quantum spin hall effect: theory and experiment. *J. Phys. Soc. Jpn.* **77**, 031007 (2008).
81. Kobayashi, S. & Furusaki, A. Fragile topological insulators protected by rotation symmetry without spin-orbit coupling. *Phys. Rev. B* **104**, 195114 (2021).
82. Chan, Y.-H., Chiu, C.-K., Chou, M. & Schnyder, A. P. Ca 3 p 2 and other topological semimetals with line nodes and drumhead surface states. *Phys. Rev. B* **93**, 205132 (2016).
83. Nielsen, H. & Ninomiya, M. Absence of neutrinos on a lattice: (i). proof by homotopy theory. *Nucl. Phys. B* **185**, 20–40 (1981).
84. Nielsen, H. & Ninomiya, M. Absence of neutrinos on a lattice: (ii). intuitive topological proof. *Nucl. Phys. B* **193**, 173–194 (1981).
85. Le, C., Yang, Z., Cui, F., Schnyder, A. & Chiu, C.-K. Generalized fermion doubling theorems: Classification of two-dimensional nodal systems in terms of wallpaper groups. *Phys. Rev. B* **106**, 045126 (2022).
86. Beenakker, C. Chiral edge mode for single-cone dirac fermions. *Phys. Rev. B* **110**, 165421 (2024).
87. Zhang, H. et al. Topological insulators in Bi_2Se_3, Bi_2Te_3 and Sb_2Te_3 with a single dirac cone on the surface. *Nat. Phys*. **5**, 438–442 (2009).

88. Acosta, C. M., Lima, M. P., da Silva, A. J., Fazzio, A. & Lewenkopf, C. Tight-binding model for the band dispersion in rhombohedral topological insulators over the whole brillouin zone. *Phys. Rev. B* **98**, 035106 (2018).
89. Song, Z. et al. In *First principle calculation of the effective zeeman's couplings in topological materials* 263–281 (World Scientific, 2022).
90. Yang, S. A., Pan, H., Yao, Y. & Niu, Q. Scattering universality classes of side jump in the anomalous hall effect. *Phys. Rev. B* **83**, 125122 (2011).
91. Lu, H.-Z. & Shen, S.-Q. Extrinsic anomalous hall conductivity of a topologically nontrivial conduction band. *Phys. Rev. B* **88**, 081304 (2013).
92. Yang, B.-J. & Nagaosa, N. Classification of stable three-dimensional dirac semimetals with nontrivial topology. *Nat. Commun.* **5**, 4898 (2014).

Acknowledgements

This work was supported by the Research Grants Council, University Grants Committee, Hong Kong under Grants No. C7012-21G and No. 17301823, the National Key R&D Program of China under Grant No. 2019YFA0308603, Quantum Science Center of Guangdong-Hong Kong-Macao Greater Bay Area GDZX2301005, and Guangdong Basic and Applied Basic Research Foundation No. 2024A1515010430 and 2023A1515140008.

Author contributions

S.-Q.S. conceived the project. B.F. performed the theoretical analysis and simulation. B.F. and S.-Q.S. wrote the manuscript with inputs from all authors. All authors contributed to the discussion of the results.

Competing interests

The authors declare no competing interests.

Additional information

Supplementary information The online version contains supplementary material available at https://doi.org/10.1038/s42005-024-01926-w.

Correspondence and requests for materials should be addressed to Bo Fu or Shun-Qing Shen.

Peer review information *Communications Physics* thanks the anonymous reviewers for their contribution to the peer review of this work. A peer review file is available.